Assessment of oceanographic conditions during the North Atlantic EXport processes in the ocean from RemoTe sensing (EXPORTS) field campaign

Leah Johnson [a,*], David A. Siegel [b], Andrew F. Thompson [c], Erik Fields [b], Zachary K. Erickson [d], Ivona Cetinic [e,f], Craig M. Lee [a], Eric A. D'Asaro [a], Norman B. Nelson [b], Melissa M. Omand [g], Michaela Sten [b], Shawnee Traylor [h,i], David P. Nicholson [i], Jason R. Graff [j], Deborah K. Steinberg [k], Heidi M. Sosik [h], Ken O. Buesseler [h], Mark A. Brzezinski [b], Inia Soto Ramos [f,g], Filipa Carvalho [l], Stephanie A. Henson [l]

[a] Applied Physics Laboratory and School of Oceanography, University of Washington, Seattle,WA, USA
[b] Earth Research Institute, University of California, Santa Barbara, CA, USA
[c] Environmental Science and Engineering, California Institute of Technology, Pasadena, CA, USA
[d] NOAA Pacific Marine Environmental Laboratory, Seattle, WA, USA
[e] NASA Goddard Space Flight Center, Greenbelt, MD, USA
[f] Morgan State University, Baltimore, MD, USA
[g] University of Rhode Island, Graduate School of Oceanography, Narragansett, RI, USA
[h] The MIT-WHOI Joint Program in Oceanography/Applied Ocean Science and Engineering, Cambridge and Woods Hole, MA, USA
[i] Woods Hole Oceanographic Institution, Woods Hole, MA, USA
[j] Oregon State University, Department of Botany and Plant Pathology, Corvallis, OR, USA
[k] Virginia Institute of Marine Science, Gloucester Point, VA, USA
[l] National Oceanography Centre, Southampton, UK

ABSTRACT

This manuscript presents an overview of NASA's EXport Processes in the Ocean from Remote Sensing 2021 Field Campaign in the North Atlantic (EXPORTS NA) and provides quantitative and dynamical descriptions of the physical processes modulating water transformations during the study. A major programmatic goal was to conduct the sampling in a Lagrangian mode so that ocean ecological and biogeochemical changes can be observed independent from physical advective processes. To accomplish this goal, EXPORTS NA conducted a multi-ship, multi-asset field sampling program within a retentive, anticyclonic mode water eddy. Beneath depths of ~ 100 m, Lagrangian sampling assets remained within the eddy core waters (ECWs) throughout the experiment, demonstrating that the ECWs within the mode water eddy were retentive. However, strong westerly winds from four storm events deepened the mixed layer (ML) of the surface core waters (SCWs) above the eddy's mode water core by 25–40 m and exchanged some of the SCWs with surface waters outside of the eddy via Ekman transport. Estimates of flushing times ranged from 5 to 8 days, with surface exchange fractions ranging from 20 to 75 % and were consistent with particle tracking advected by combined geostrophic and Ekman velocities. The relative contributions of horizontal and vertical advection on changes in ECW tracers depended on the horizontal and vertical gradients of that tracer. For example, horizontal advection played a large role in ECW salinity fluxes, while vertical entrainment played a larger role in the fluxes of nutrients into SCW ML. Each storm injected nutrients and low oxygen waters into the ML, after which the surface ocean ecosystem responded by reducing nutrient concentrations and increasing %O_2 saturation levels. Overall, ECW values of chlorophyll and POC were the largest at the onset of the field program and decreased throughout the campaign. The analysis presented provides a physical oceanographic context for the many measurements made during the EXPORTS NA field campaign while illustrating the many challenges of conducting a production-flux experiment, even in a Lagrangian frame, and the inherent uncertainties of interpreting biological carbon pump observations that were collected in a Eulerian frame of reference.

1. Introduction

The ocean's biological pump transports organic carbon, created by photosynthetic plankton, from the surface ocean into the interior, where it can be sequestered for months to millennia (DeVries, 2022). There are three primary export pathways connecting the surface ocean with the interior- the gravitational sinking of organic particles, the physical advection and mixing of suspended particles and dissolved organic matter, and active transport by vertically migrating zooplankton and other metazoans (Boyd et al. 2019; Siegel et al. 2023). Together these

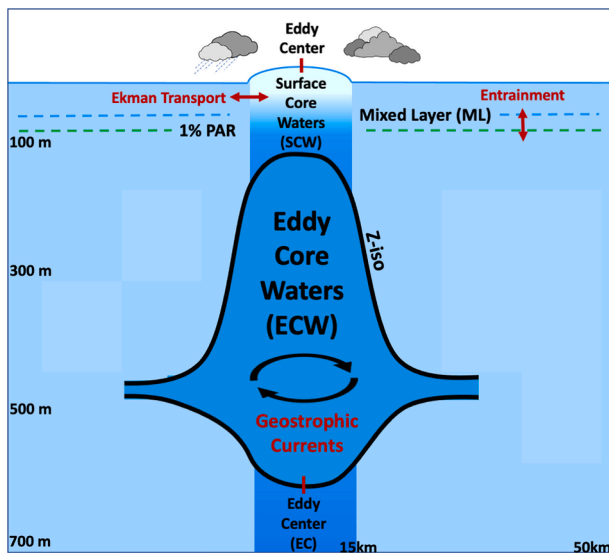**Fig. 1.** Conceptual diagram of the anticyclonic eddy (A2) sampled during the EXPORTS NA deployment illustrating the locations of the surface core waters (SCW) and eddy core waters (ECW) and the basic physical processes affecting their interactions (red) with each other and the surrounding ocean. Approximate mean locations are shown here for the mixed layer depth, the euphotic zone depth (1% PAR) and the depth of the 27.15 isopycnal surface (z_{iso}). These properties are shown in greater detail in the analyses to follow. (For interpretation of the references to color in this figure legend, the reader is referred to the web version of this article.)

pathways transport roughly 10 Pg of organic carbon from the surface ocean each year, although the predictive understanding of these pathways and their variations in time and space remains limited (e.g., Nowicki et al. 2022; Siegel et al. 2023). The goals of NASA's EXport Processes in the Ocean from Remote Sensing (EXPORTS) Field Campaigns are to develop these predictive abilities and to assess their impacts in contemporary and future climates (Siegel et al. 2016). The EXPORTS Field Campaigns aims to address three core science questions: 1) How do the three export pathways transport organic matter from the surface ocean? 2) What controls the efficiency of that transfer below the well-lit surface ocean? 3) How can the knowledge gained from these field campaigns reduce uncertainties in estimates of the fate of marine organic carbon?

To answer these questions, EXPORTS conducted two major, multi-platform field deployments in contrasting ecosystems. The first was conducted in the Subarctic North Pacific Ocean near Ocean Station P (August-September 2018; Siegel et al, 2021). This high nutrient, low chlorophyll site can be characterized as a highly recycled, low export ecosystem where organic matter was tightly retained in the surface-ocean mixed layer and zooplankton populations mediated much of the transport of organic matter to depth (Stamieszkin et al. 2021; Steinberg et al. 2023; McNair et al 2023). The recent EXPORTS North Atlantic Ocean deployment (EXPORTS NA; May 2021) was conducted to provide a contrasting end member by focusing on the export associated with the North Atlantic spring bloom where all three export flux pathways are likely to be important (Dam et al 1993; Omand et al, 2015; Martin et al. 2011). EXPORTS NA is the focus of this manuscript.

A major operational goal of the EXPORTS science plan was to conduct core food web rate and export flux determinations in a Lagrangian frame of reference to minimize the influence of advective processes on their interpretation (Siegel et al. 2016). During the North Pacific EXPORTS field campaign, the weak horizontal currents and spatial gradients in biogeochemical fields and low level of temporal variability that characterize the fall season at the Ocean Station P site made this goal achievable to a large degree (Siegel et al. 2021; McNair et al. 2023).

However, in the North Atlantic, advective processes are much more active and advection by both mean and eddying circulations can cause upper ocean biogeochemical properties to evolve on time and space scales comparable to those driven by biological processes (e.g., Mahadevan et al. 2012; Omand et al. 2015; Mousing et al. 2016). Further, there were operational considerations with deploying and recovering a large array of autonomous platforms in a highly advective environment combined with the need to maximize science returns from the research ships while minimizing the time spent recovering the autonomous assets.

In an attempt to alleviate the influences of advective processes, the EXPORTS NA field program was conducted within a well-defined mesoscale eddy. Since their potential vorticity is conserved, mesoscale eddies are expected to be retentive. Targeting such a retentive mesoscale feature required an extensive eddy tracking endeavor before the intensive in situ observational phase. Eddy tracking also allowed for adaptive real time sampling strategies to maximize science returns. A description of this process is documented in Erickson et al. (2022) and Erickson et al. (2023). Within the moving reference frame of the eddy, an array of research vessels and autonomous sampling platforms were tasked with either following the eddy center, obtaining a semi-Lagrangian view of biogeochemical evolution, or capturing the spatial variability of physical and biogeochemical tracers that characterized the feature and region surrounding it.

The selected feature, (A2 as in Erickson et al, 2022, 2023; referred to here as 'the eddy'), was a small (diameter of the core region was ~ 30 km) anticyclonic feature that was located approximately 170 km due east of the site of the Porcupine Abyssal Plain Observatory (PAP-SO; Hartman et al., 2021). The feature had strong anticyclonic circulation with descending isopycnal surfaces from its edge to the eddy center below ~ 600 m (Fig. 1); however, above this depth, there were upward sloping isopycnals that characterized the eddy core. The region between the diamond shaped isopycnals is the eddy core waters (ECW). The depths of the top isopycnal surfaces helped identify the eddy's surface core waters (SCW) within the mixed layer (ML). Identifying SCWs in the data is described in detail in section 4b, and is schematized in Fig. 1.

From here on, core and ECWs refer to the deeper eddy structure, while SCWs are in the mixed layer (ML) only. This distinction is important, as the deeper eddy structure and surface waters of the eddy evolved differently and the SCWs are within the ML where the bulk of the biogeochemical sampling was conducted. Of particular importance is characterizing the retentiveness of the eddy's SCWs and quantifying horizontal advective changes in SCW properties is essential for assessing the degree to which the observations are Lagrangian. Furthermore, small scale horizontal variability of ML properties is inherent in energetic regimes such as the North Atlantic as will be shown below. It is therefore necessary to evaluate the tendency of mean SCW biogeochemical properties $(\overline{C})$ as

$$\partial\overline{C}/\partial t \ = \ HORIZ + VERT + NetBGC + ERROR \qquad (1)$$

where *HORIZ* refers to the net exchange of surface waters via ageostrophic processes like Ekman transport and horizontal stirring, *VERT* summarizes the net exchanges of materials with subsurface waters via entrainment as well as air-sea exchanges, *NetBGC* reflects the net biogeochemical changes in the property in question and *ERROR* represents the uncertainty level in the measurements, analyses and theory. *HORIZ* and *VERT* are assumed to encapsulate physical advective processes only.

The characterization of the net biogeochemical changes independent of physical forcings (i.e. *NetBGC* above) is a major objective of the EXPORTS Science Plan. Here, we will show that despite the retentiveness of the ECWs in the eddy's interior, several large storm events, strong mesoscale currents, and ageostrophic flows contribute to changes in the mean SCW properties via advective and mixing processes. Our goal is to describe the physical backdrop of the field site and to identify and
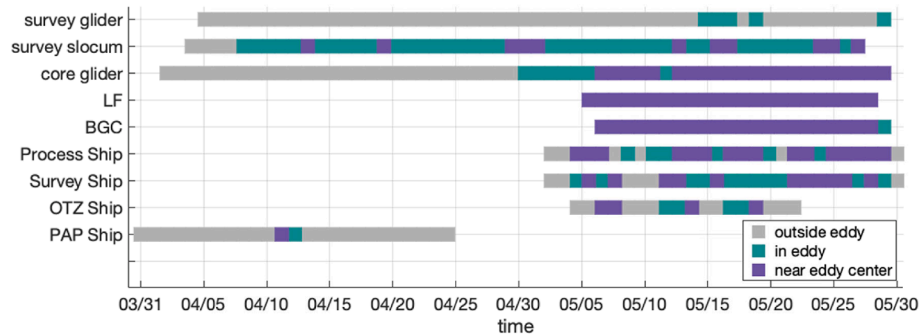
Fig. 2. Timeline of vessels and autonomous assets used throughout this analysis in terms of their location; outside the eddy (gray), inside the eddy (within 80 km of the eddy center; green) and near the eddy center (within 15 km of eddy center; blue). The National Oceanography Centre's annual cruise to the PAP Observatory aboard the RRS Discovery (DY130) deployed three gliders that surveyed the broader eddy field prior to the EXPORTS NA field campaign. The main sampling efforts occurred between May 4, 2021 and May 30, 2021. Three autonomous assets (core BGC, LF, and core SG) and the process ship (JC214) were dedicated to sampling near the eddy center. Two other gliders (survey SL and survey SG), the survey ship (DY131), and OTZ ship (SG2105) sampled across the eddy. Other assets deployed during the campaign can be found in Appendix A. (For interpretation of the references to color in this figure legend, the reader is referred to the web version of this article.)

Table 1
Epoch Time Boundaries.

Epoch 1	Epoch 2	Epoch 3
May 4–10, 2021	May 11–20, 2021	May 21–29, 2021

quantify the physical oceanographic advective and mixing processes that alter SCW properties.

This contribution presents an overview of the oceanographic setting during the EXPORTS North Atlantic field campaign. The goal is to describe the environment during and immediately prior to the intensive observation phase and to provide metrics for understanding how the physical environment impacted the ecological and biogeochemical stocks and rates observed. In particular, the selection of an eddy center as a Lagrangian field site will be evaluated, addressing important contextual questions including:

- What was the physical and biogeochemical framework of the EXPORTS NA deployment site and how did it vary in space and time?
- What were the conditions before intensive sampling occurred and how did these conditions influence the observations made?
- How Lagrangian (i.e. retentive) were the surface and interior waters of the selected eddy?
- How did temporal variations in external surface forcing (i.e. storms) affect the physical and biogeochemical environment?
- How can these findings inform future field studies of the biological carbon pump?

2. The EXPORTS NA field campaign

2.1. Sampling strategy

The EXPORTS NA campaign focused on quantifying the pathways that govern the transport of organic carbon from the euphotic zone into the mesopelagic in a region of energetic mesoscale and submesoscale physical variability. The presence of strong fronts, eddies and filaments that evolved on timescales of hours to days provided the potential for significant physical transport of carbon, yet also provided the challenge of resolving biological and physical export processes in an environment dominated by advection. For example, the mesoscale eddy field rapidly separates nearby surface water parcels, with simulations suggesting separations of hundreds of kilometers over the course of a month (Lehahn et al. 2007). This dispersion was limited by making the biogeochemical stock and rate measurements within the core of a single mesoscale eddy that remained coherent and water-retaining throughout

the measurements.

An array of ship-based and autonomous sampling platforms was tasked with one of two main objectives, those tasked with semi-Lagrangian sampling within a target eddy center, and those aimed at sampling the spatial variability within and around the eddy. A list of the ships, autonomous vehicles, and sampling capabilities can be found in Appendix A, and a subset of these platforms particularly relevant to describe the physical backdrop is summarized here. A Lagrangian float (LF), a BGC Argo float (core BGC) and a seaglider (core SG) were dedicated to sampling the eddy center, providing consistent reference measurements for studies conducted by the Process ship (RRS James Cook) focused on ecological rates, BGC fluxes, temporal changes in the food web, and optical properties. The Survey ship (RRS Discovery), along with two gliders, a seaglider (survey SG) and a Slocum glider (survey SL) sampled the surrounding eddy fields (Fig. 2). Additionally, the EXPORTS NA collaborated with the Ocean Twilight Zone project (OTZ) ship (R/V Sarmiento de Gamboa), which collected a variety of measurements both within and around the eddy. Further, the National Oceanography Centre's annual cruise to the PAP Observatory deployed the three gliders and collected hydrographic profiles and samples for analysis from the PAP site and the eddy prior to the EXPORTS NA field campaign.

The ship-based science teams worked closely with a shore team through a comprehensive situational awareness plan for coordinated adaptive sampling strategies. A shore-based server linked ships and shore databases, allowing for a steady stream of updated asset location and real-time measurements, including remote (e.g. satellite fields) and in-situ (e.g. glider and shipboard ADCP, underway and CTD data) data fields. In addition to data availability, formal and informal communication lines were established on the situational awareness server, through email, and through instant messaging platforms.

Similar to the EXPORTS NP field program, the ship-based sampling strategy revolved around "epochs", designed to have sampling durations long enough to allow export pathway measurements yet short enough for sampling to be in a semi-Lagrangian framework. For EXPORTS NP, epochs were about 8 days. During the EXPORTS NA field program, sampling strategies were punctuated by several storm events that required ships to move considerable distances away from the eddy and interrupted sampling. These storm events naturally set the epoch boundaries (Table 1).

2.2. Sensor intercalibration process and results

Finescale variation in physical and biogeochemical properties underlines the need for careful intercalibration of sensors from ship-based
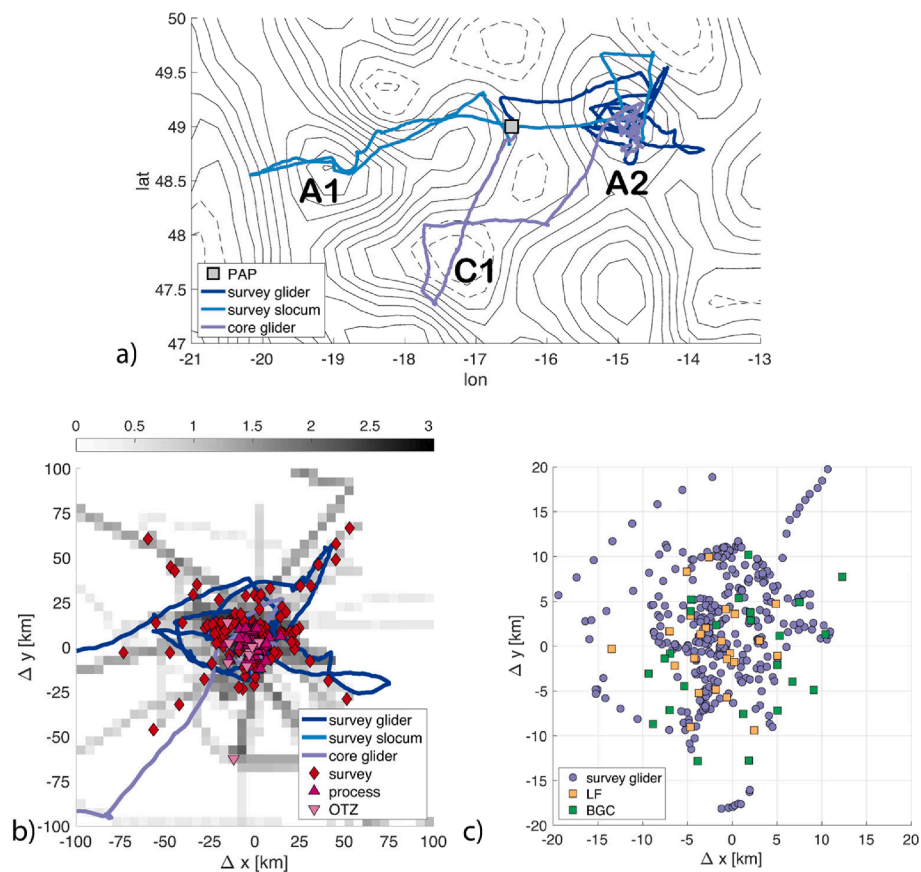
Fig. 3. Maps of field program sampling. a) glider surveys from April 1, 2021 to May 30, 2021. Gliders were deployed by the NOC ship near the Porcupine Abyssal Plain Sustained Observatory (PAP-SO) (gray square) and were tasked with surveying the potential target eddies (A1, A2, andC1) prior to the ship-based field campaign. The field campaign focused on a single eddy, A2, nominally centered at 14.6 W and 48.8 N. Contours are positive sea level anomaly (solid) and negative sea level anomaly (dashed) for May 4th 2021. b) Heat map of ships transects, overlaid with the glider tracks (lines) and the locations of shipboard CTD casts (markers) in eddy center reference frame. c) Location of core asset profiles in the eddy center reference frame.

and autonomous platforms. Multiple, dedicated intercalibration profiles between various sensor platform pairs were included as part of the field program design, with a goal of near-simultaneous vertical profiles collected at spatial separations less than 1 km. "Opportunistic" calibration casts were also identified and used. Measurements collected from the CTD on the survey ship established the basis for the intercalibration, allowing us to directly correct temperature and salinity properties from the other two ships (process ship and OTZ ship), the three ocean gliders (core SG, survey SG, survey SL), the BGC Argo floats (core BGC), and the Lagrangian float (LF). Due to small spatial scale variability in the ML, the determination of offsets between sensors was most effective when comparing the subsurface, well-mixed core properties of the eddy (typically between 300 and 500 m), if measured by both sensors. Typical offsets were negligible for temperature sensors and < 0.01 psu for salinity sensors, except the survey SG which had a large salinity offset. The same calibration casts were used to intercalibrate dissolved oxygen, chlorophyll fluorescence, and optical backscattering properties. Full details of the intercalibration approach are provided in Siegel et al. 2023. The Gibbs Sea-water toolbox (TEOS-10; McDougall and Barker, 2011) was used to convert calibrated data into conservative temperature (T), absolute salinity (S), potential density (σ_0), spice (Π), and % O_2 saturation (from hereon %O_2). POC was estimated from optical backscatter using the relationship for the NA as determined by Cetinić et. al. (2012).

2.3. Site choice and eddy tracking

The ability to identify an appropriate eddy and track it in real time

before and during the field program was paramount to the success of the EXPORTS NA goals. Months before the beginning of the ship-based sampling, a broad satellite data survey of the PAP region of the North Atlantic was conducted to characterize mesoscale eddies and assess the likelihood that they would be long-lived and retentive (Erickson et al. 2022; 2023). The principal method for identifying and tracking the eddies before the ship-based program employed satellite altimetry data and associated geostrophic velocities. Simulated particle trajectories were initialized within eddies and advected with satellite derived geostrophic velocities for up to 60 days. We used data from multiple years and assessed the average lifespan of a particle within each eddy as a measure of how retentive the eddy was. Eddy size and previous retentiveness were found to be the strongest predictors that a given eddy would remain coherent and retentive for the following 30–60 days, matching the duration of the EXPORTS NA deployment (Erickson et al. 2022; 2023).

Remote sensing observations of eddy size, retentiveness, and geographic location were used to identify three target regions (two anticyclonic eddies [A1 & A2] and one cyclonic eddy [C1]; see Fig. 3) for pre-campaign glider surveys (Erickson et al. 2022). The pre-survey was crucial for final eddy identification, as the vertical structure of the subsurface revealed by the gliders could be compared against the satellite-based metrics. For example, dynamic height from C1 was very weak, suggesting a weak subsurface eddy-like signature. Alternately, the depth-averaged currents from A1 revealed a highly energetic eddy with a circulation that was not well defined by altimetry. Fortunately, in-situ fields of depth-averaged currents and geostrophic height for the eddy A2 agreed with altimetric fields. The agreement between in-situ fields and
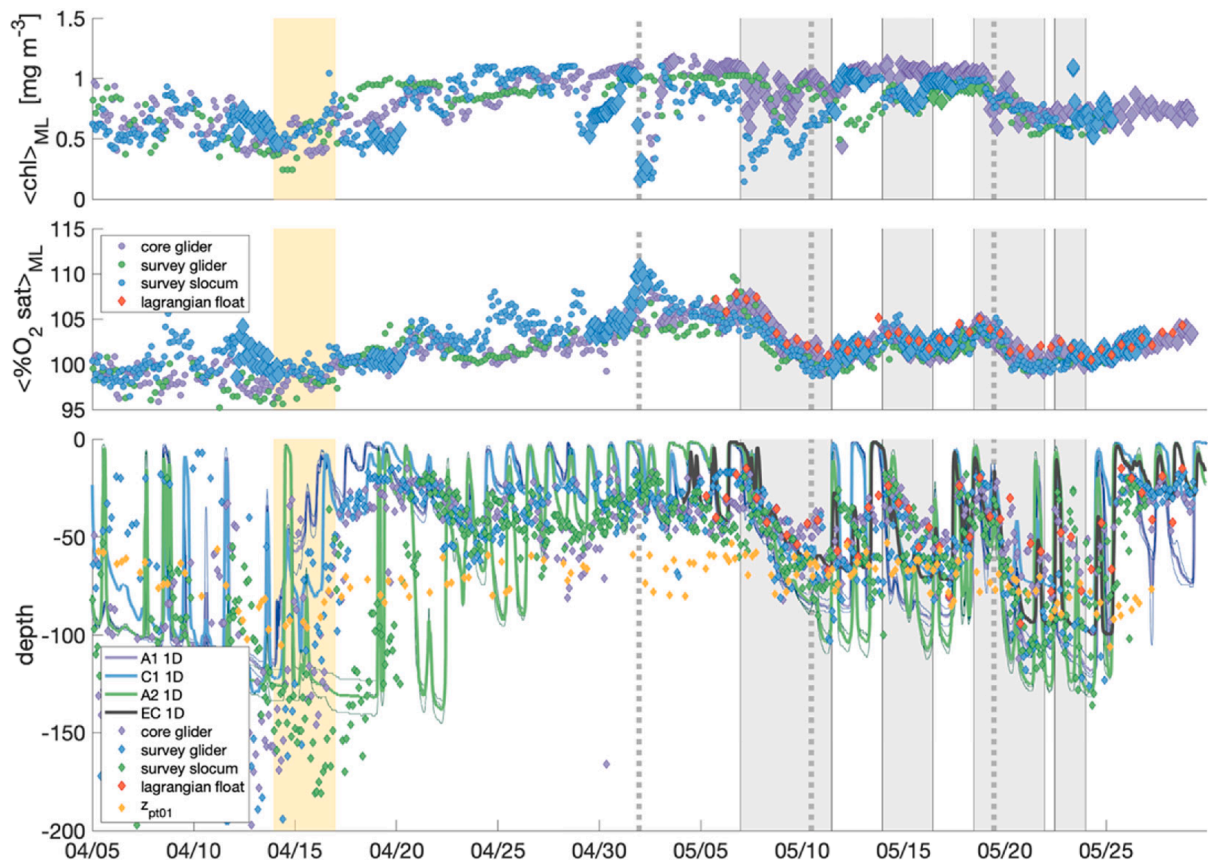
Fig. 4. Broader North Atlantic environment before the field program. a) chlorophyll and b) %O₂ as measured by the three gliders. Gliders surveyed a range of territory (see Fig. 3). Larger diamonds denote times when that specific glider was within 15 km of the eddy center. c) MLD from gliders (diamonds) and from 1D model ensembles (lines) forced with ERA data at the locations of A1, C1 and A2 and with in-situ data for the eddy center (See Appendix B). The bold lines are the mean of the ensemble and thin lines are the standard deviation of the ensemble. Also included are the 0.01 % PAR light levels (yellow diamond). In all panels, the yellow shaded region bound the time period of the heat flux zero crossing (determined using ERA net heat flux), the gray dashed lines delineate campaign epochs and the gray shaded regions highlight the four storm events. (For interpretation of the references to color in this figure legend, the reader is referred to the web version of this article.)

satellite-based metrics generated confidence that eddy A2 would be retentive and easily tracked by satellite for the duration of the campaign.

A dedicated shore team tracked the eddy with in-situ and satellite fields, providing a daily eddy center location product. The eddy product depended on the previous seven days of shipboard ADCP measurements to define an ensemble of eddy centers based on two methods, a) minimization of an objectively mapped streamfunction and b) the location which was maximally tangential to the horizontal velocity measurements (see Erickson et al., 2022, 2023). From here on, the use of 'eddy center' refers to this product location. The onset of the ship-based field program began with the deployment of the LF near the eddy center. Both the data-based eddy center and LF location were used to guide ship-based and autonomous platform sampling.

Satellite-based estimates of the eddy center diverged from those estimated from ADCP horizontal velocities by about 10 km. Post-campaign, a daily eddy center ensemble product was constructed as above using ADCP data that was taken in a 5-day window centered on the day in question (Erickson et al., 2022). The success of the core assets at following the targeted eddy center estimate can be seen in the sampling patterns of the three autonomous core assets; the LF, core BGC and core SG, with 87 % of the total core asset profiles being within 15 km of the eddy center.

3. Pre field campaign conditions

A previous NOC field program in the PAP region (PAP ship in Fig. 2; RSS Discovery, cruise DY130), combined with glider observations and

1D models (See Appendix B) provides an account of the region before the intensive field campaign (Fig. 4). The PAP ship collected nutrients at the PAP site as well as at the eddy (A2) between April 10–12. While the gliders surveyed three eddies in the region throughout April (e.g. Fig. 3). Across the basin, surface values of NO_3 and SiO_4 ranged from 7 to 8 M L⁻¹ and 3.1–3.5 M L⁻¹, respectively. Elevated Chl and %O₂ values suggest that primary productivity was occurring, yet the presence of elevated ML macronutrients and deep MLs (~100 m) suggest the spring phytoplankton bloom may not have occurred yet.

All three gliders were deployed near the PAP in early April with the task of surveying three potential eddy candidates (Figs. 2 & 3). Surface fluxes of heat and momentum from ERA-5 (Hersbach et al. 2020) analysis were used to force 1D models (see Appendix B) near the locations of the glider surveys.

Early in April, surveying gliders saw highly variable ML depths across the domain (glider sampling spanned ~ 400 km; Fig. 3) with possible mixing extending to 250 m depth, well below the 0.1 % PAR level depth of 60–70 m (Fig. 4). Periodic ML shoaling occurs during this time, with evidence of dynamical lateral restratification known to inhibit mixing during the spring transition (e.g. Mahadevan et al 2012, Johnson et al, 2016).

By April 15th, the surface heat flux from ERA-5 predicted a zero crossing (Fig. 4), one metric for North Atlantic bloom initiation (e.g., Rumyantseva et al. 2019), and MLs began to shoal above the 0.1 % light level, whereafter Chl levels did increase. By April 17, MLs were less than 40 m in the western eddies, while a storm event to the east kept the target eddy center well mixed until April 22nd. By April 27th, one week
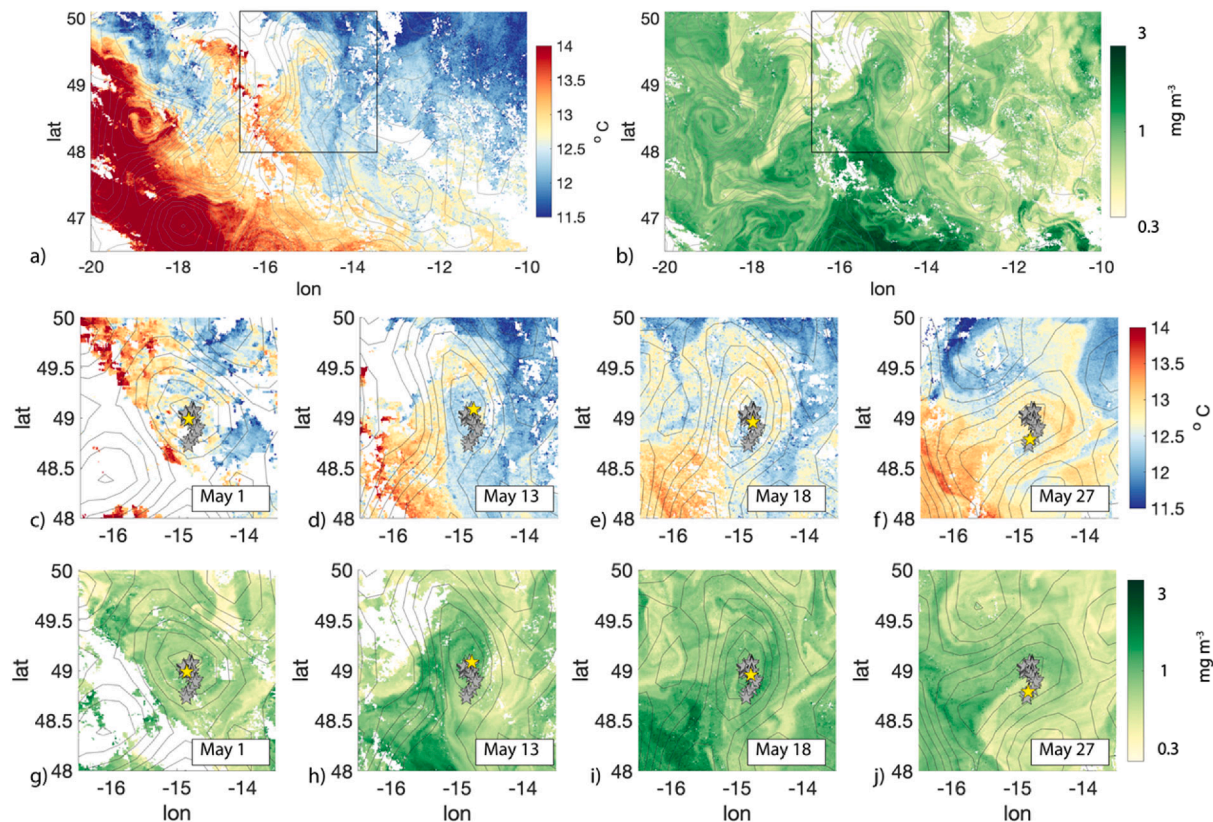
Fig. 5. Daily composite satellite sea surface temperature (a, c-f) and chlorophyll *a* concentrations (c, g-j) for the study region. All figures include sea level anomaly contours (2 cm intervals). The top row shows the broader eddy fields on May 13th, with horizontal heterogeneity in both SST and Chlorophyll-a. Boxes in a) and b) highlight the eddy and outline the bounds of maps (c-j). The middle row (c-f) and bottom row (g-j) are a close-up of the eddy for specific dates throughout the field program. In these lower panels, gray stars represent all daily post-processed eddy centers during the field program, and the yellow star represents the eddy center for the date plotted. (For interpretation of the references to color in this figure legend, the reader is referred to the web version of this article.)

before the field program began, weather was calm and MLs observed by the gliders across the region had shoaled to ~ 30 m, well above the 0.1 % PAR level. During this same period, Chl concentrations near the center of eddy A2 rose and remained high until the beginning of the ship observations in early May. The agreement between models and observations, as well as the buildup of temperature stratification observed across glider profiles supports the importance of solar warming for the shallow MLs in the second half of April. The onset of the field program began within this springtime shallow mixed layer environment.

4. Characterizing the target eddy

The EXPORTS NA field program targeted center of a coherent, mesoscale eddy to reduce the effects of horizontal advection on the time series observations. While the sampling focused near the eddy's center, understanding exchanges between the eddy interior and its environs is critical for interpreting changes in the observed biogeochemical and ecological properties. Here, we focus on the physical characteristics of the target eddy to provide context for future analyses of the coupled physical-biogeochemical-ecological processes.

4.1. Eddy environment and structure

In situ observations show distinct hydrographic properties that distinguish the surface waters near the eddy center from surrounding waters at both the surface and at depth. At large scales (hundreds of km), surface properties are characterized by a transition from warm and salty waters south and west of the eddy to cold and fresh waters to the north and east (Fig. 5a). The anti-cyclonic circulation that defines eddy A2 stirred this background tracer gradient, causing warmer waters to the

south to be wrapped around the eddy periphery throughout the sampling period (Fig. 5b). This stirring created mesoscale (>O(10 km)) gradients in temperature and salinity, although these gradients were largely density compensating, a characteristic of the North Atlantic basin (e.g. Thompson et. al., 2016). A combination of high-resolution ocean color images (Fig. 5c) and altimetry-derived finite size Lyapunov exponents suggest that smaller-scale (1–10 km) gradients are generated, especially around the periphery of the eddy, in part due to the strong strain field (Zhang et al. 2019).

Multiple glider transects across the eddy and shipboard sampling provide a robust image of the study site. The density distribution within the target eddy has a classical mode water structure. Stratification is elevated from the base of the ML to a depth of roughly 200 m (Fig. 6a). Between 200 and 700 m, the eddy is distinguished by weak vertical stratification, or a "mode" of water with low potential vorticity (PV; defined as $f N^2$); this region defines the ECWs. Within the eddy, water properties are largely homogenized with a compact distribution in temperature and salinity space and a potential density change of only 0.05 kg m^{-3} across the 500 m-thick core (Fig. 6a,b).

Between depths of 200 and 500 m, isopycnals slope downward moving away from the center, with the steepest tilt (strongest geostrophic shear) between 10 and 30 km from the eddy center. Below 500 m, isopycnals tilt upward moving away from the eddy center, which partially compensates for the positive sea surface height (SSH) anomaly (Fig. 1, Fig. 6c,d). Geostrophic shear in the upper 400 m of the water column acts against the background anticyclonic circulation. The vertical stratification is dominated by temperature (Fig. 6c) with strong along-isopycnal salinity variations (Fig. 6d) on density surfaces below the eddy core.

The structure of the eddy evolved during the observational program,
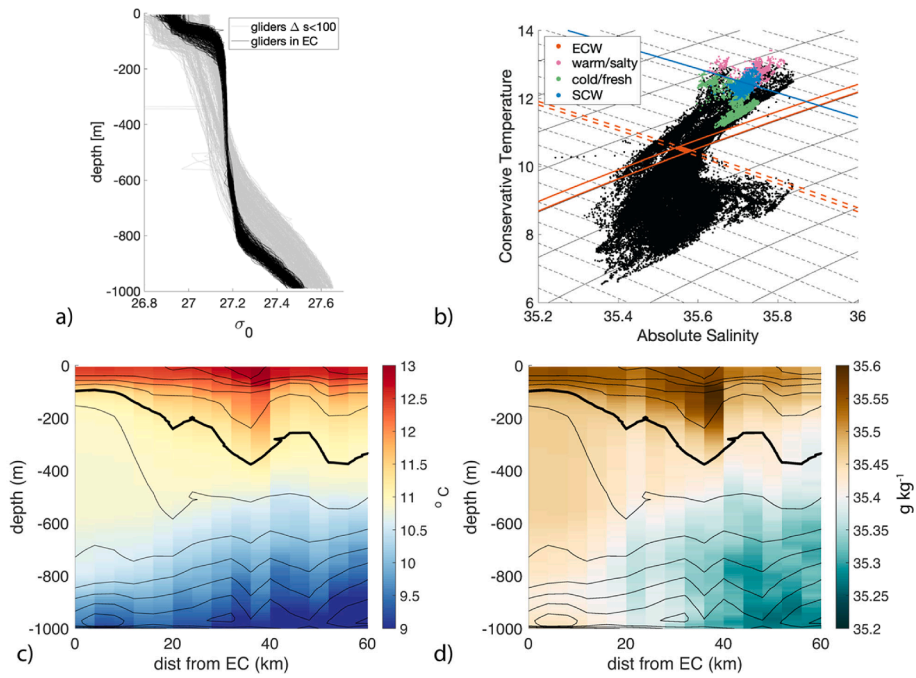
Fig. 6. Eddy structure and composition. a) Potential density profiles from all three gliders within a 100-km radius of the eddy center (gray) and only the glider profiles within 15 km of EC (black; see Section 4b). b) T/S diagram for all glider profiles collected within 100 km of the eddy center. Contours are σ_0 (solid) and Π (dashed). The eddy low PV core waters (orange) comprise a small portion of T/S space. ML water classes are separated into core (blue), warm/salty (pink) and cold/fresh (green). The orange spice and potential density contours define the core waters and the blue spice contour separates the surface water classes that are not classified as SCWs. See Section 4 for details. Profiles from all gliders were used to construct composite radial maps of c) conservative temperature and d) absolute salinity. Composite plots include $z_{iso} = 27.1$ kg m^{-3} (dark line), and 0.5 kg m^{-3} contours (thin black lines). (For interpretation of the references to color in this figure legend, the reader is referred to the web version of this article.)
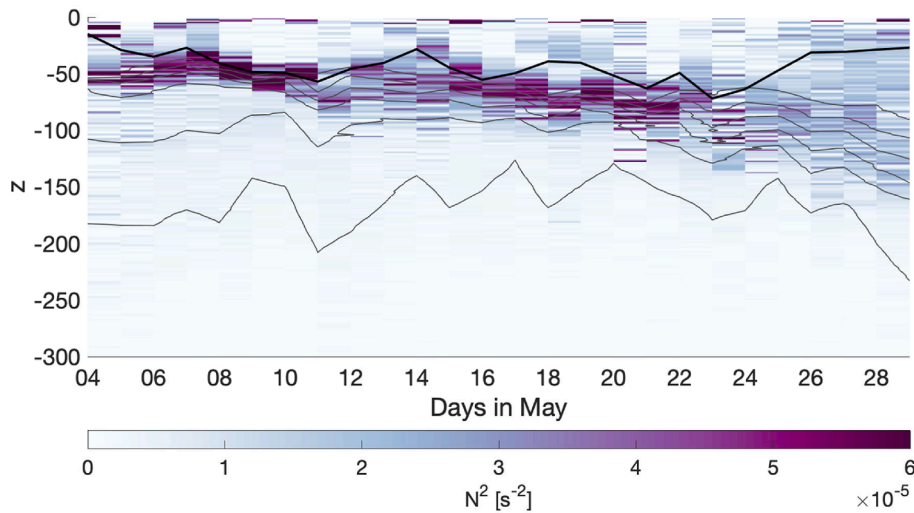
Fig. 7. - Daily averaged N^2 from profiles within 15 km of EC. Grey lines are 0.3 kg m^{-3} density contours and black line is the MLD. Strong N^2 at the ML base gets deeper and more diffuse towards the end of the field program.

with initial circular SSH contours that become oblong towards the end of Epoch 3 (see progression in Fig. 5c-f). During this evolution, the low PV core remained intact, but the strength of the pycnocline between the surface waters and the low PV core weakened (Fig. 7).

4.2. Water mass classification

The identification of water mass classes can be used to evaluate the degree to which waters sampled near the eddy center were Lagrangian and their definition leverages the physical traits of the eddy. The strong

retentive core waters of the eddy are uniform in T/S, yet the surface waters above the core are highly variable. Therefore, water mass classification focuses on identifying two regions: a) the retentive ECWs associated with the low PV layer, and b) the SCWs which occupy ML waters above the retentive ECWs.

i) Eddy Core Waters

The ECW class is defined from spice, (Π), and potential density, σ_0, (GSW-10), where Π is a metric of the density compensating warm-salty
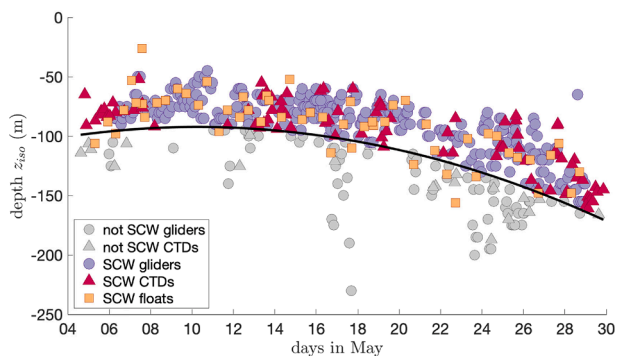
Fig. 8. z_{iso} - The depth of the 27.1 kg m^{-3} isopycnal for all profile data collected within 15 km of the eddy center. Black line is a quadratic fit threshold used to define SCW, z_{iso}^{fit} − 15 m. The quadratic fit to z_{iso} for data collected within 15 km of the eddy center is z_{iso}^{fit} = -0.203x^2 + 2.543x − 100 where x is day in May 2021. Profile data with z_{iso} above this threshold is considered to have ML waters in the SCWs. E.g. SCW glider, SCW CTD, and SCW float are all data collected within 15 km of EC and have a z_{iso} shallower than z_{iso}^{fit}. Note that not all data collected within 15 km of EC satisfy this criterion (gray icons) and highlights the importance of using vertical structure to identify a profile's location within the eddy.

vs. cold-fresh traits of the water. Spice and density space is a convenient transformation of temperature and salinity space (McDougall and Barker, 2011) and is particularly useful in density compensated circulations such as the North Atlantic. The low PV (low stratification) ECW is defined by potential density, 27.150 < σ_0 < 27.195 kg m^{-3}, and spice 1.63 < Π < 1.65 kg m^{-3} (orange lines in Fig. 6b). Though this definition spans a small range of the possible T-S observed across the eddy, it isolates a large portion of water mass observed, spanning a height of ∼ 500 m near the eddy center and up to 20 km radius at a depth of 600 m. In the upper 400 m, the core is colder and fresher than the surrounding waters. The strong retentive ECWs persisted throughout the campaign, verified by the core SG which profiled to 1000 m four times a day (Fig. 6a). Variability in T and S increases radially from the core, consistent with eddy stirring evident in Fig. 5.

ii) Surface Core Waters

Semi-Lagrangian sampling by the process ship and the core assets targeted the eddy center. Defining the SCW class is therefore important, both to identify which samples were collected in the waters above the retentive eddy core (see Fig. 1) and to characterize the evolution of those waters over the course of the sampling period. While the strong retentive ECW are uniform in T and S, and therefore easily identifiable, the surface waters above the ECW are considerably more variable in both space and time due to lateral stirring and vertical mixing. For example, T and S variability predicted by 1D ML models (see Appendix B) spans 0.7 °C and 0.04 g kg^{-1} respectively, about 40 % of the variability observed by the core SG within 15 km of the eddy center, complicating our ability to use T and S as markers of a specific ML water class. Therefore, SCWs are defined as surface waters above the low PV eddy core.

For profile data (i.e. profiling assets and CTD casts), the SCW class is defined by the depth of the 27.1 isopycnal (z_{iso}), the isopycnal that sets the upper bound on the low PV layer (Fig. 6). A quadratic fit to data collected within 15 km of the eddy center (z_{iso}^{fit}; Fig. 8) shows that the depth of z_{iso} deepens with time, consistent with a weakening pycnocline (Fig. 7). From this, SCWs are defined by profiles with a z_{iso} shallower than z_{iso}^{fit} minus 15 m (e.g. 15 m deeper than z_{iso}^{fit}; Fig. 8). For underway data (nominal depth of 5 m) the SCW is labeled as being within 15 km of the eddy center product. About 86 % of profiles within 15 km of the eddy center are designated SCWs. Finally, surface waters that did not classify as SCW were partitioned into a warm salty water class, or a cold fresh

water class defined by a Π threshold of 2.1 (the average spice of the SCWs over the entire sampling period). Surface water characteristics and the resulting water mass classifications illustrate the complex surface water swirling around the eddy (Fig. 9).

It is important to recognize that the T/S space occupied by the SCW is not as well defined as it is for the ECW, despite SCW having much less volume (Fig. 6b). This SCW variability, which is a result of the large-scale background gradients and small unresolved T/S gradients (Figs. 5 & 9), as well as water mass transformation (i.e., *VERT* and *HORIZ* in Eq. (1)), obfuscates the physical and biogeochemical landscape. Therefore, it is helpful to focus on the evolution of mean characteristics of the SCWs. Since SCWs occupy approximately a region within 15 km of the eddy center, it is assumed that the "resolved" scales are approximately 30 km. It will be shown that storm driven entrainment and ageostrophic Ekman transport (*VERT* and *HORIZ* in Eq. (1), respectively) modulate T/S variability in the SCWs. This insight will be used to describe the evolution of physical and biogeochemical tracers in the SCW and surrounding surface waters.

## 5. Surface core water temperature and salinity budgets

5.1. Surface forcing and mixed layer entrainment

Near-surface hydrographic and biogeochemical properties respond to atmospheric forcing and ML entrainment fluxes (1D processes) as well as lateral transport. To assess the relative importance of 1D (vertical) dynamics during the ship samplings, we compare the observations to an ensemble of single-column mixing models (Appendix B), forced with both ship-based meteorological measurements and ERA-5 reanalysis (Fig. 10). ML-averaged T/S and mixed layer depths (MLD, defined using a 0.03 kg m^{-3} density threshold; de Boyer Montégut et al, 2004), estimated from a combination of 1D models and profiling assets, describe the evolution of the upper ocean during the campaign.

Due to the passage of several storms prior to the arrival of ships, ML properties had a complex evolution (see Fig. 4). The surveying gliders observed ML shoaling 1–2 weeks prior to the ship-based field program (Section 3). After the arrival of the survey ship and process ship, four storms throughout May brought high westerly winds (Table 2) that deepened MLs at the field site during each event (Fig. 10c). ML deepening, Δ H, during storms ranged from roughly 20 to 45 m and resulted in post storm ML depths (H_f) ranging from 56 to 80 m (Table 2). The entrainment velocity, $w_E = \partial H / \partial t$, where H is the MLD, ranges from 10 to 35 m day^{-1}; here, values of w_E are calculated by locally estimated scatterplot smoothing (LOESS) using daily MLs observed by the core SG (Table 2). Between storm events, MLs shoaled to ∼ 30 m as low winds and surface warming reduced upper ocean mixing. Periods designated as storm days (11 in total) account for 42 % of the field program and play a leading order role in the budgets of passive and biogeochemical tracers.

The extent of ML deepening during each storm depends on the magnitude of surface wind and buoyancy forcing, the initial stratification at the ML base, and storm duration (Table 2). The relative importance of momentum and buoyancy fluxes on ML deepening is captured by the non-dimensional ratio L_{MO}/H, where $L_{MO} = (\tau/\rho_0)^{3/2}/B_0$ is the Monin-Obukov length (Monin and Obukov, 1954). The reference density, ρ_0, is set as 1025 kg m^{-3}, τ is the wind stress, and the surface buoyancy flux is B_0 = -($\alpha g/\rho_0 c_p$) Q_{NET} - ($\beta g S_0$) PME, where α is the thermal expansion coefficient, β is the haline contraction coefficient, *g* is gravitational acceleration, PME is precipitation minus evaporation, and S_0 is a reference salinity of 35 g kg^{-1}. B_0 is positive during cooling and negative during warming and freshwater fluxes. When $|L_{MO}/H|$>1, wind-driven shear dominates mixing at the ML base (all storms). When $L_{MO} > 0$ (i.e. $B_0 > 0$), wind and cooling act in concert to generate mixing (storm 2), and when $L_{MO} < 0$ (i.e. $B_0 < 0$), wind mixing acts against surface warming (storms 1, 3 and 4). During all four storms, $|L_{MO}/H| \sim$ 2–50, indicating the dominance of wind-driven deepening during each storm event (Table 2). The largest Δ H occurs during storm 1, as four
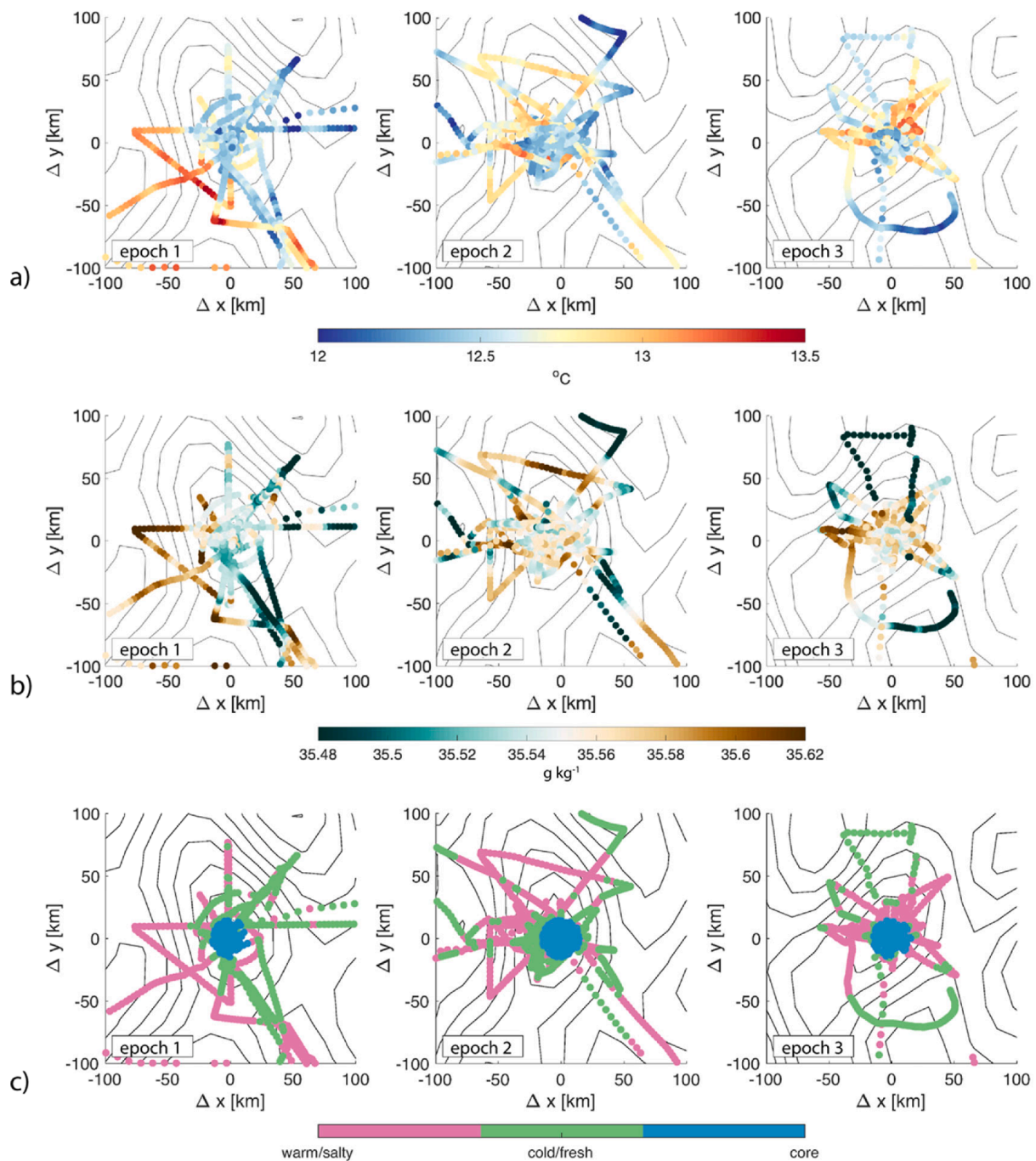
Fig. 9. A) sea surface temperature, b) sea surface salinity and c) surface water mass identification during epoch 1 (left), epoch 2 (center), and epoch 3 (right). spatial data is plotted in the eddy center reference frame (distance from eddy center). each figure contains data from the process ship and survey ship underway, as well as surface (~5m) data from the core SG, survey SG, and survey SL.

days of high winds act against a modest restratifying surface buoyancy flux to erode the stratification that built up over the previous weeks (Section 3). This first storm event significantly impacted the physical and BGC quantities of SCWs (Sections 5b, 5c and 6).

In summary, change in ML T/S properties due to 1D processes (i.e. *VERT* in Eq. (1)) is the result of surface forcing and ML entrainment. Entrainment caused SCW cooling during the storms, despite a warming net heat flux ($Q_{NET} > 0$) during storms 2 and 3. During storm 1, a slight salinification of the ML can be attributed to the entrainment of deep high salinity anomaly. Subsequent deepening events generally freshened the ML. These processes are captured by the 1D models; yet it will be shown that the 1D models do not sufficiently explain the observed T/S tendency

of SCWs, suggesting the role of spatial variability and horizontal advection on SCW properties.

5.2. Impact of lateral advection on surface core waters

The SCWs (defined by z_{iso} and generally within ~ 15 km of the eddy center) were not horizontally uniform, with spatial variability occurring both within the SCWs and across the eddy (see Section 4, Fig. 9). Horizontal transport can be divided into resolved (horizontal mean) and unresolved (small-scale) processes using Reynolds averaging. For example, the impact of horizontal advection on changes in mean SCWs can be written as:
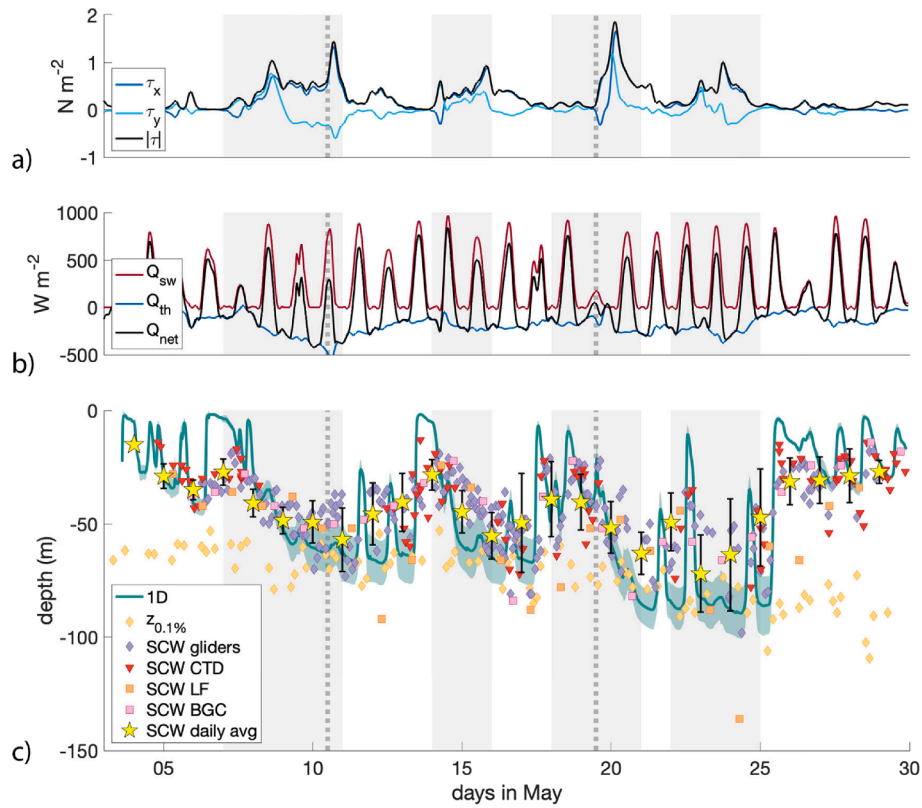
Fig. 10. Surface Forcing and ML evolution at EC over the duration of experiment, where epoch boundaries are depicted as vertical gray dotted lines, and storm periods highlighted in light gray. a) total wind stress magnitude (black) along with northward wind stress (light blue) and eastward wind stress (dark blue), consistent with southwesterly winds. b) total Q_{NET} (black) along with net shortwave heat flux (red) and thermal heat fluxes (blue). c) MLDs from models and observations. The 1D model mean MLD (teal) is plotted with the ensemble std error (teal shaded). Markers include all SCW designated profiles from gliders (purple diamonds), CTDs (red triangles), and the LF and BCG floats (orange and pink squares respectively). The daily mean and std of all SCW assets are also included (yellow stars). Yellow diamonds show the 0.1% par levels as measured from the core SG. (For interpretation of the references to color in this figure legend, the reader is referred to the web version of this article.)

Table 2

Surface forcing and ML quantities during storm events - Including storm dates (Dates), storm duration (Duration), ML change during each storm (Δ H), final ML after each storm (H_f), entrainment velocity (w_E), average turbulent diffusivity in ML from 1D models (κ), avg heat flux (Q_{NET}), avg wind stress (τ), net freshwater flux (PME), and the ratio between Monin-Obukhov depth and ML depth(L_{MO}/H).

	Storm 1	Storm 2	Storm 3	Storm 4
Dates	5/7–5/10	5/14–5/15	5/18–5/20	5/21–5/22
Duration	4 days	2 days	3 days	2 days
Δ H	46.5 m	25.5 m	35.5 m	34.1 m
H_f	68 m	56 m	70 m	80 m
w_E	10.3 m day^{-1}	10.2 m day^{-1}	17.7 m day^{-1}	34.1 m day^{-1}
κ	2.0 x10^{-3} m^2 s^{-1}	2.1 x10^{-3} m^2 s^{-1}	5.0 x10^{-3} m^2 s^{-1}	0.5 x10^{-3} m^2 s^{-1}
Q_{NET}	−41.8 W m^{-2}	66.0 W m^{-2}	2.7 W m^{-2}	−11.1 W m^{-2}
τ	0.46 N m^{-2}	0.42 N m^{-2}	0.57 N m^{-2}	0.59 N m^{-2}
max wind speed	44 knts	37 knts	50 knts	42 knts
PME	1.5x10^{-7} m s^{-1}	2.1x10^{-7} m s^{-1}	2.4x10^{-7} m s^{-1}	−3.7x10^{-7} m s^{-1}
L_{MO}/H	−54	2	−7	−2

$$HORIZ = U \nabla \overline{C} + \nabla \cdot \overline{u'C'} \qquad (2)$$

On the right-hand side, the first term is the advection of the mean tracer gradient by the mean horizontal geostrophic and ageostrophic flow (i.e. resolved, see Section 4b), and the second term is assumed to be the unresolved submesoscale transport contribution. At strong lateral gradients (e.g. the edges of mesoscale eddies) submesoscale flows can

play an important role in both lateral and vertical transport. Though evidence of fine-scale structure in the SCW supports the existence of submesoscale variability (e.g. Figs. 5 & 9), submesoscale transport by $\nabla \overline{u'C'}$ is notoriously difficult to quantify in observations and its estimation is outside the scope of this work. The rest of this section will focus on the advection of tracers by larger-scale currents captured by $U \cdot \nabla \overline{C}$ and will highlight the importance of ageostrophic Ekman flows in transporting tracers into the SCWs.

The impact of horizontal advection on the mean SCW salinity and temperature tendencies can be estimated by subtracting the changes due to 1-D processes (*VERT*) from the observed changes in time, $\partial \overline{C}/\partial t$, in equation (1), or

$$HORIZ = \partial \overline{C}/\partial t \ - VERT + ERROR \qquad (3)$$

Observed daily salinity and temperature tendencies ($\partial \overline{C}/\partial t$) were determined by using a two-day LOESS regression fit to each core asset (core SG, LF, and core BGC). The vertical component of the tendencies (*VERT*) was determined using an ensemble of 1D models (see section 5a, Appendix B). Although ERROR cannot be measured explicitly, it represents the uncertainty in the models and observations. For *VERT*, the uncertainty is estimated using the standard deviation (STD) among the ensemble of models. For the tendency term, $\partial \overline{C}/\partial t$, uncertainty is estimated as the STD among core assets. Finally, the residuals between $\partial \overline{C}/\partial t$ and *VERT* across core assets give estimates of daily horizontal advection (*HORIZ*) into the SCWs (Fig. 11b & c) along with an uncertainty of that estimate (error bars).

During storm events 1–3, the SCWs became warmer and saltier than can be explained by surface forcing and entrainment alone (Fig. 11b &
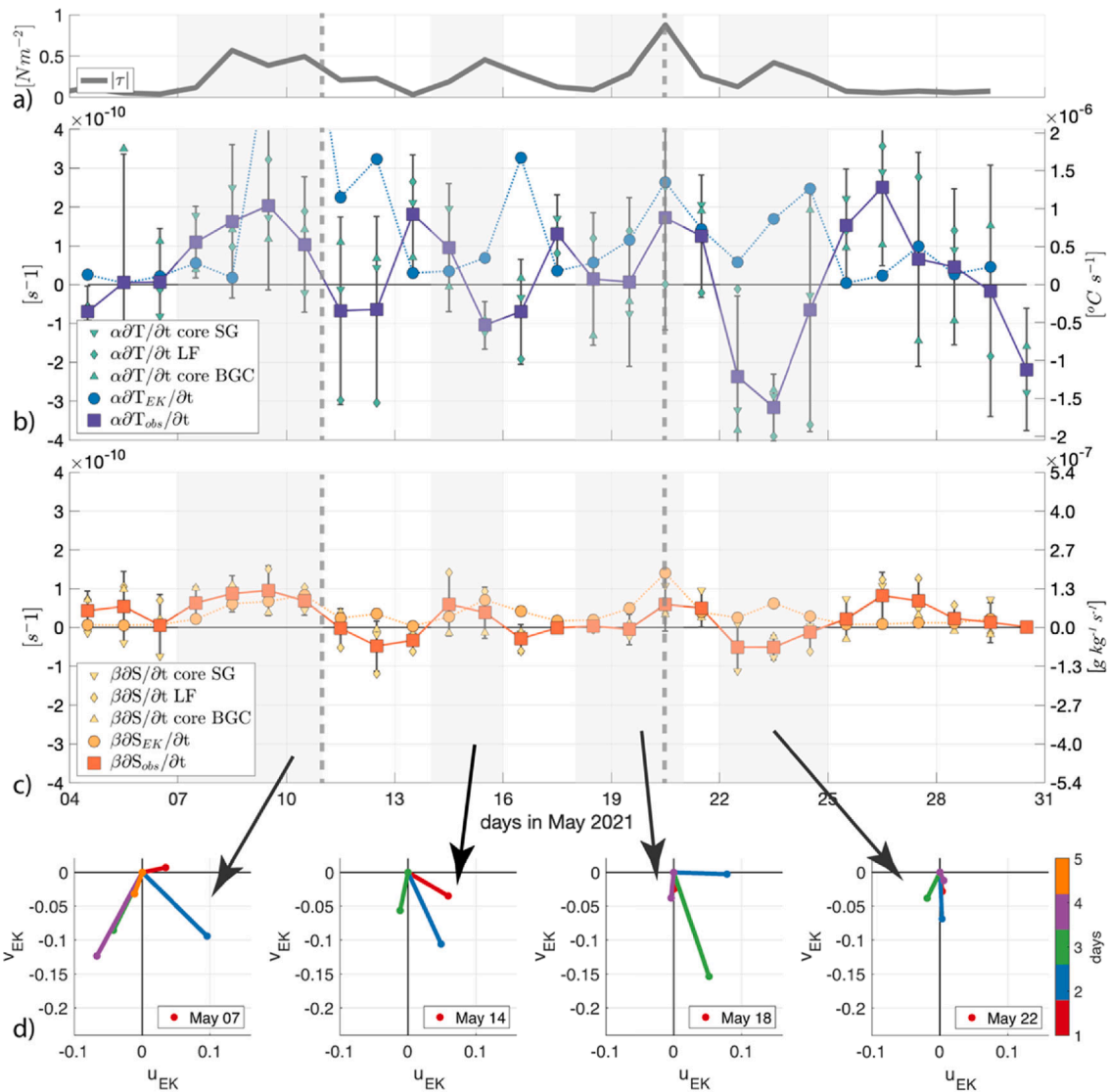
Fig. 11. Terms contributing to temperature and salinity budgets. a) wind stress magnitude. b) Estimates of horizontal temperature advection from observations and 1D models (blue circles) and Ekman transport (blue squares). c) Estimates of horizontal salinity advection from observations and 1D models (orange circles) and Ekman transport (orange squares). In both b) and c), error bars represent the combined spread from 1D models and across observational platforms. The tendencies are normalized by α and β respectively (left axis) to show that both tracers have a leading order role on changes in density, with temperature having a larger role. Dimensional ranges are included on the right axis. Estimates of horizontal advection tend to be larger during the storm events (shaded regions) as evident in the magnitude of the wind stress (gray). (d) Daily Ekman velocities during each storm are represented in stick plots where the south-westerly winds result in Ekman transport to the southeast. The red sticks correspond to the dates in each legend, and subsequent days of the storm follow the colorbar on the right. (For interpretation of the references to color in this figure legend, the reader is referred to the web version of this article.)

c). A cooling and freshening during storm event 4, followed by a salinification on May 26 can be attributed to aliased sampling within the eddy (i.e. sampling a saltier region of the SCWs, possibly a submesoscale filament). The aliased sampling does not come as a surprise considering the complexity of the region and reinforces the usefulness of spatial averaging to determine SCW properties. Integrating *HORIZ* over the entire 28-day field program suggests that a total of Δ T = 0.42 °C and Δ S = 0.012 g kg^{-1} of the observed change cannot be explained by 1D processes. Comparing this with the integrated changes due to *VERT* (i.e. surface forced dynamics and entrainment) of Δ T = 0.22 °C and Δ S = -0.03 g kg^{-1}, suggests that both *VERT* and *HORIZ* have leading order roles on the ML T/S budget.

Eddy stirring by the background anti-cyclonic circulation is evident in the evolution of satellite SST (Fig. 5), as well as the evolution of water classes during each epoch (Fig. 9). The closed contours of the altimetric geostrophic streamlines suggest a retentive eddy center, as confirmed by

the well-defined and unchanging ECW thermohaline water properties. However, near the surface, strong westerly winds during the four storm events induce an ageostrophic Ekman transport that exchanges SCWs with the surrounding eddy surface waters. This would be represented in the first term on the right-hand side of Eq. (2) as:

$$HORIZ_{EK} = U_{EK} \cdot \nabla \overline{C} \qquad (4)$$

where $\nabla \overline{C}$ is the horizontal gradient in the direction of the Ekman transport. The daily Ekman velocities have a magnitude of $U_{EK} = \tau/(Hf\rho_0)$, where f is the local Coriolis frequency. Estimates of the spatial gradients, $\partial \overline{C}/\partial s$, must balance the need for sufficient data across the eddy, while also minimizing aliasing related to temporal changes. To accomplish this, surface fields of temperature and salinity (from ship underway data and profiling assets) are separated by epoch Table 1) and spatial gradients of temperature and salinity are calculated in the direction of U_{EK} using a LOESS regression fit. Estimates of $HORIZ_{EK}$ (Fig. 11b & c)
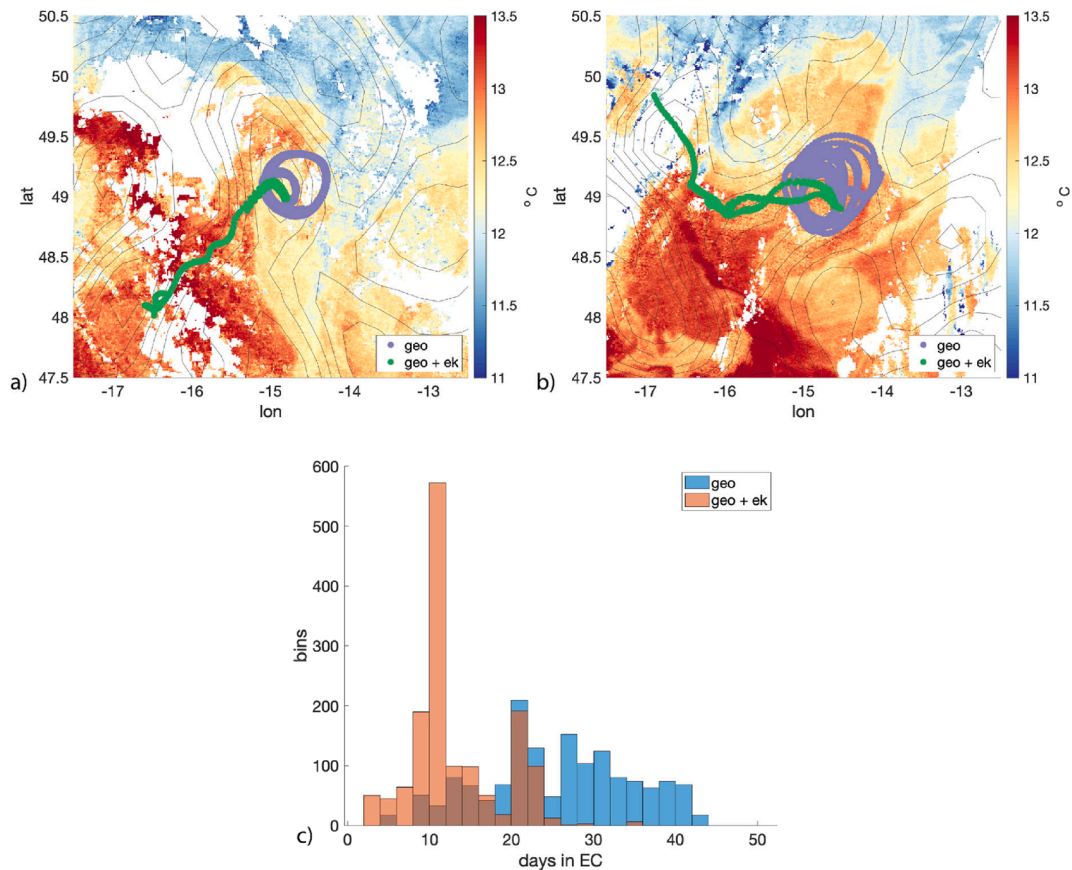
Fig. 12. Difference in particle trajectories advected by geo and geo + ekman velocity fields. Top plots: SST and 25 day particle back trajectories advected with geostrophic velocities (geo, purple) and with a combination of geostrophic velocities and Ekman velocity (geo + ekman, green particles). a) SST from May 13th 2021, and particle trajectories initiated on May 10th. b) SST from May 27th 2021, and particle trajectories initiated on May 24th. Because of the limited satellite data, SST and particle dates are offset, with SST chosen for sufficient coverage and particle trajectory initiation dates chosen to capture storm events. c) Histogram of particle retention in eddy at the time of initiation. The average particle retention was 25 days for geo and 12 days for the geo + ek. (For interpretation of the references to color in this figure legend, the reader is referred to the web version of this article.)

suggest Ekman currents transport warm salty water into the SCWs.

The relative contributions of *HORIZ* and *VERT* on T/S changes suggest that horizontal fluxes play the dominant role in T/S tendencies in the SCW (Fig. 11b & c). For the first three storms, the correspondence between $HORIZ_{EK}$ and the residual between $\partial \overline{C}/\partial s$ and VERT for SCW salinity values is especially compelling (Fig. 11c) as both imply storms advect salty water into the SCWs. This is attributed, in large part, to the strong horizontal lateral gradients in T/S that are a feature of the energetic North Atlantic. Translating these results to other physical and biogeochemical variables will depend on the relative strength of the vertical and horizontal gradients (see Section 6b on BGC entrainment fluxes). The ability to constrain *VERT* and *HORIZ* is a result of successful sampling strategies during the field campaign. However, disagreements between the $HORIZ_{EK}$ and the residual between $\partial \overline{C}/\partial s$ and VERT (i.e., error bars in Fig. 11b & c) point to aliased sampling, calculation errors (as discussed above) and/or the influences of unresolved processes and highlights the challenges of interpreting observational data in such a complicated region.

5.3. 5c retention times of surface core waters

Advection of warm salty water into the SCWs by eddy stirring and Ekman transport is investigated further using particle tracking analysis based on two different velocity fields: 1) geostrophic velocities (u-geo) and 2) geostrophic velocities with Ekman transport (u-geo-ek), both provided by Copernicus Marine Service CMES. It is assumed that u-geo is representative of velocities associated with the first baroclinic mode (i.e.

ECWs) and u-geo-ek more accurately captures currents in the near surface, biologically active upper ocean (i.e. SCWs). Initial positions and times for the particle tracking were chosen based on locations of SCW CTD casts from the Survey Ship. Particles were advected backward for 20 days using a Runge-Kutta method (Fig. 12).

Particles advected with u-geo have circular trajectories and remain in the eddy, suggesting that an ECW particle at the time of sampling had been in the eddy core for the previous 20 days. Particles advected by u-geo-ek tell a different story and indicate that the sources of SCWs can have origins outside of the eddy. Ekman currents can cause surface particles to deviate from geostrophic streamlines (i.e. lines of constant sea level anomaly, SLA; Fig. 12a & b), especially during storm events. As the geostrophic anticyclonic circulation transports warm salty water from the southwest around the Eddy periphery, south-westerly winds advect that warm salty water into the SCWs. The nonlinearity of the geostrophic currents in an eddying regime can create chaotic flow fields (e.g. MacGilchrist et al. 2017). Here, the evolving eddy circulation combined with intermittent storms and Ekman transport accentuate the chaotic nature of surface flows during the field campaign, with SCW origins from the southwest earlier in the campaign and from the northwest later in the campaign. The combination of Ekman and geostrophic surface flows reduces retention times of particles near the eddy center (Fig. 12c), with an average u-geo-ek particle retention of 12 days compared to a 25-day retention for u-geo particles. This further supports the disconnect between the retentive deeper ECWs (Section 4, Fig. 6) and the SCWs, with the latter subject to complicated water mass exchanges and transformations.

Table 3

Flushing timescales for storms. Time required to replace waters over a 15-km circle for each storm event (see discussion in section 5c).

	Storm 1 (end epoch 1)	Storm 2 (during epoch 2)	Storm 3 (epoch 2 to 3)	Storm 4 (during epoch 3)
Timescale flush (days)	5.5	5.3	6.3	8.5
% SCWs flushed	73 %	38 %	47 %	23 %

Table 4

Mean and standard deviations for SCW ML variables for each epoch.

	Epoch 1	Epoch 2	Epoch 3
Conservative Temperature (°C)	12.4 ± 0.2	12.5 ± 0.2	12.5 ± 0.2
Absolute Salinity (g kg^{-1})	35.69 ± 0.01	35.72 ± 0.01	35.72 ± 0.01
Spice (kg m^{-3})	2.11 ± 0.04	2.15 ± 0.07	2.16 ± 0.05
Chl (mg m^{-3})	1.04 ± 0.14	0.93 ± 0.10	0.66 ± 0.06
POC (μmol L^{-1})	8.2 ± 1.6	6.7 ± 0.9	5.1 ± 0.7
% O$_2$	103.9 ± 2.2	102.5 ± 1.0	102.1 ± 1.4
NO$_3$ (μmol L^{-1})	4.9 ± 0.1	4.7 ± 0.4	5.5 ± 0.3
SiO$_4$ (μmol L^{-1})	0.2 ± 0.1	0.5 ± 0.3	1.5 ± 0.2
bSi (μmol L^{-1})	1.8 ± 0.2	0.7 ± 0.2	0.4 ± 0.3
MLD (m)	38.7 ± 11.7	43.9 ± 14.4	42.9 ± 18.7

A flushing time scale for SCWs can be estimated as the amount of time required for an Ekman driven current to displace a 15 km radius circle (Table 3). Using this rough calculation, 73 % of surface waters 15 km from the eddy center were replaced during storm 1, consistent with the jump in salinity for SCWs between epoch 1 and epoch 2 (Fig. 11b, Table 4). Particle tracking (Fig. 12) suggests that waters in the eddy at the beginning of epoch 2 may have exchanged with waters up to a radius of 80 km from the EC and with origins within the warm salty filament west of the eddy. Subsequent storm events resulted in smaller exchanges of SCWs.

6. Biogeochemical tracers

6.1. Tracer evolution

The degree to which a Lagrangian framework was achieved by conducting the study in a retentive anticyclonic feature was presented in the last section, based on a budget analysis of physical properties, with the conclusion that during the four storm events, wind driven Ekman flows transport warm/salty water into the SCWs. This section draws on the analysis of the physical fields to understand the evolution of the biogeochemical and optical properties within 15 km of the eddy center). Both the physical and biogeochemical environment were sampled continuously by the three autonomous core assets (LF, core SG, and core BGC) and sporadically from CTD casts from the process, survey and OTZ ships. Shown in Fig. 13a-f are the temporal evolution of eddy center properties, including conservative temperature, absolute salinity, chlorophyll concentration, POC concentration, %O$_2$ saturation, and nitrate concentration. Agreement across observational platforms is a product of the careful adaptive sampling strategies and rigorous intercalibration efforts described in Section 2.

The physical oceanographic properties within the ECW (below ∼ 200 m) were largely homogenous and unchanging (Fig. 13). For example, a LOESS in time for ECW salinity between 300 and 350 m is O (10^{-10}) g kg^{-1}s^{-1}, 3 orders of magnitude less than changes seen in the SCW. Above the ECWs, there is considerable variability in the thermohaline properties in the SCW (Fig. 13 a,b). These changes were largely due to the intense storm events driving Ekman transport replacing a fraction of the SCWs (Section 5c), as well as changes due to vertical ML entrainment events. Generally, the contribution of horizontal advection, surface forcing and vertical entrainment to T/S were equivalent in

magnitude, though at times, competing in sign. When evaluated over the three sampling epochs, an increase in SCW temperature and salinity is apparent from epoch 1 to epoch 2, while mean SCWs do not change between epochs 2 and 3 (Table 4). MLD (solid black line in Fig. 13) varied from less than 20 m to nearly 100 m throughout the cruise. In particular, there are signatures of vertical detrainment events temporarily depositing surface ML waters just beneath the ML with events starting on May 13, 17 and 25. With the exception of the last detrainment event, these waters were reincorporated with the surface ML as the ML deepens. Last, the region just below the ML but above 200 m showed a good deal of variability in thermohaline properties. Warmer temperature events correspond with higher salinity values, possibly due to spatial variability in the eddy center and isopycnal heaving. In this depth region, the thickness of the thermocline /halocline grows in time as shown in Fig. 7.

Variations in biogeochemical properties (Fig. 13c-f) reflect both changes related to the physical oceanographic processes described previously and those driven by biological processes. The discussion of these data here is not meant to be exhaustive but rather is intended to set the stage for focused analyses of these coupled processes in subsequent manuscripts. SCW ML values of Chl, POC, and %O$_2$ all decreased from epoch 1 to 3, illustrating that sampling caught the demise of the North Atlantic spring bloom as was planned (Fig. 13c-e; Table 4). ML nitrate and silicate concentrations both increased throughout the experiment (Table 4). These increases were likely due to the remineralization of organic matter and the entrainment of higher NO$_3$ and SiO$_4$ (and lower %O$_2$) values from depth during storm events. Below the ML, values of Chl, POC and %O$_2$ are smaller than their ML values and comparatively little variability is observed within the ECWs. As with the physical fields, signatures of vertical detrainment events occur and temporarily suspend biogeochemical tracers beneath the mixed layer. For example, enhanced levels of Chl, POC, and %O$_2$ were present below the shoaled ML starting on May 13, 17 and 25.

Spatiotemporal variations in ML averaged quantities of Π, %O$_2$, Chl-a, POC, NO$_3$, PO$_4$, SiO$_4$, and bSi over the entire sampling domain, denoted by water mass (SCW, warm/salty, and cold/fresh), are shown in Fig. 14. Throughout the cruise, spatial gradients in spice dominate the variability over temporal gradients. This is not the case with any of the biogeochemical fields which, overall, experience larger changes over time than across water masses, especially after the first epoch (SCW ML mean and standard deviation values for each epoch are summarized in Table 4).

The temporal evolution of the biogeochemical data fields reflects biotic and abiotic processes. The ships arrived at the site at what appears to be the end of a large bloom. Relatively high nitrate concentration (NO$_3$ ∼ 4.8 μmol/L) but extremely low silicate concentrations (SiO$_4$ ∼ 0.2 μmol/L) suggest that the bloom was dominated by diatoms (Sieracki et al 1993). Ample nitrate remained to support an additional bloom of non-silicified phytoplankton. This dual-phase bloom scenario is typical of the North Atlantic spring bloom, as seen during the JGOFS North Atlantic Bloom Experiment (NABE, Sieracki et al. 1993, Locthe et al. 1993) and 2008 North Atlantic Bloom Experiment (Cetinić et al. 2015, Alkire et al 2014), as well as other studies in that area (e.g., Henson et al. 2006, Leblanc et al. 2009). During the first epoch, Chl, bSi and POC were at the highest levels observed during the entire field campaign (∼1.2 mg m^{-3}, bSi average E1 and 8.2 μmol/L respectively) and the ML was supersaturated in oxygen (∼105 %). The elevated bSi levels also suggest that a bloom had recently terminated in the SCWs compared with those outside of the eddy prior to the field campaign. The first epoch ended with the storm on May 8, which was associated with the largest advection and entrainment events observed during EXPORTS NA.

The evolution of biogeochemical properties for the remainder of the field campaign is influenced by storm events and variable MLs, in addition to biological and chemical processes. It appears that the weakening of mixing between storms acts as a reset for biological productivity. This can be seen most clearly in %O$_2$ (Fig. 14b), where storm-
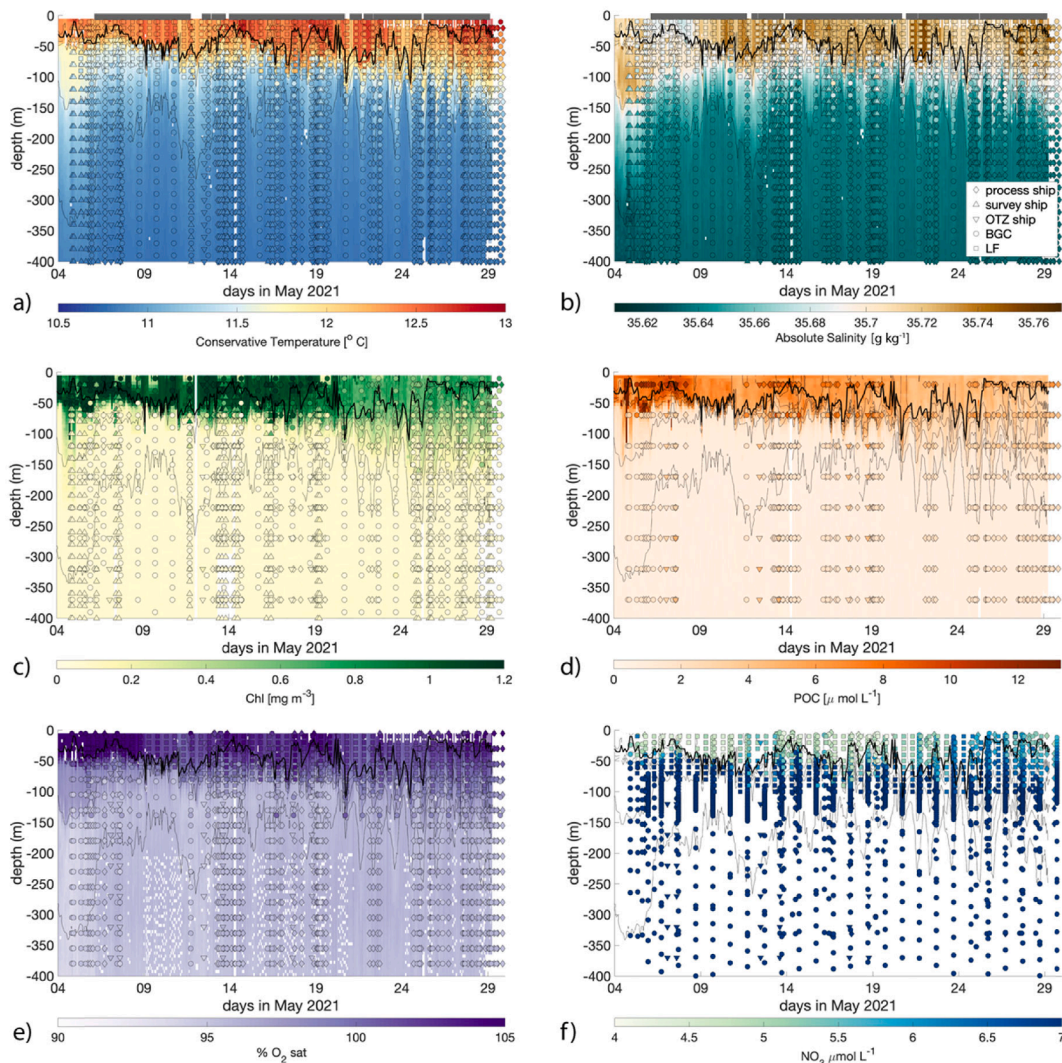
Fig. 13. Evolution of eddy center physical, optical biogeochemical observations for a) conservative temperature (^{o}C) and b) absolute salinity (g kg^{-1}), c) chlorophyll concentration (mg/m^{-3}($-$|-)), d) POC concentration (μ mol/L), e) % O$_2$ saturation, f) NO$_3$ concentration (μ mol/L). The background fields in panels (a-e) are profiles from the core SG (i.e. all fields except NO$_3$). Glider profiles designated as being within SCWs are marked by the gray lines at the top of a) and b). For example, the core SG was not sampling SCWs before May 6th, as well as around May 12th, which is consistent with warmer and saltier water between 100 and 200 m. Samples collected in the eddy center (i.e. SCW profiles only) from the process ship, survey ship and OTZ ship CTDs, the LF and the BGC are given by circles overlaid on the background fields. The dark black contour denotes the MLD measured by the core SG; the thin gray contours are 0.3 kg m^{-3} σ_o.

driven entrainment drives down oxygen, followed by increases in oxygen saturation during intermittent quiescent periods and towards the end of the experiment (epoch 3). The NO$_3$ evolution (Fig. 14e) has a similar, although inverse to %O$_2$, behavior, with increases during storm events and decreases during quiescent periods and at the end of epoch 3, likely due to biological uptake. SiO$_4$ and PO$_4$ respond similarly to NO$_3$ during epoch 1, but consumption during other epochs and storms is less clear.

Though storm modulation is seen in all water masses, spatial variability suggests different ecosystem dynamics across the eddy. This variability is largest in epoch 2, with the introduction of warm salty waters elevated in POC and depleted in NO$_3$ and PO$_4$, yet elevated in SiO$_4$ relative to the SCW. In epoch 3, variability in SiO$_4$ is lower, demonstrating a further increase in SiO$_4$ concentration across all water masses. All biomass parameters (Chl-a, POC and bSi) trended downward during epochs 2 and 3 with POC and Chl-a leveling off or increasing slightly at the end of the cruise. Overall, temporal variability across epochs in the SCW biogeochemical parameters is larger than spatial variability across water classes within any one epoch and are particularly related to the storm events.

6.2. Quantifying entrainment of biogeochemical tracers

The storms were periods where exchange between SCWs and waters outside the eddy occurred via Ekman transport as described in section 5. The storms also enabled the vertical entrainment of nutrients into the ML as can be clearly seen in the ML biogeochemical parameters (Fig. 14). This section explores the impacts of storm driven entrainment on changes in SCW NO$_3$, SiO$_4$ and PO$_4$. The change of an average ML quantity $\overline{C}$ results from the flux of that quantity across the ML base that is then thoroughly mixed (e.g. Kraus and Turner 1967). Integrating over the ML, the change of any variable $\overline{C}$ due to entrainment is:

$$\Delta\overline{C}_{ENT}/\Delta t \sim 1/H_f \ (\kappa_H*\partial\overline{C}/\partial z) \sim 1/H_f \ (\Delta H_E^2/\Delta t*\partial\overline{C}/\partial z) \qquad (5)$$

written in a flux form and bulk form respectively. In the flux form, H_f is the final ML depth after each storm, κ_H is the turbulent vertical eddy diffusivity evaluated at the ML base and $\partial\overline{C}/\partial z$ is the gradient below the ML. In the bulk form, ΔH_E is the thickness of the entrained layer and Δt is the time it took to deepen the ML (such that $\Delta H_E/\Delta t$ is the entrainment velocity, w$_E$, in Table 2). Entrainment rates can be difficult to estimate as
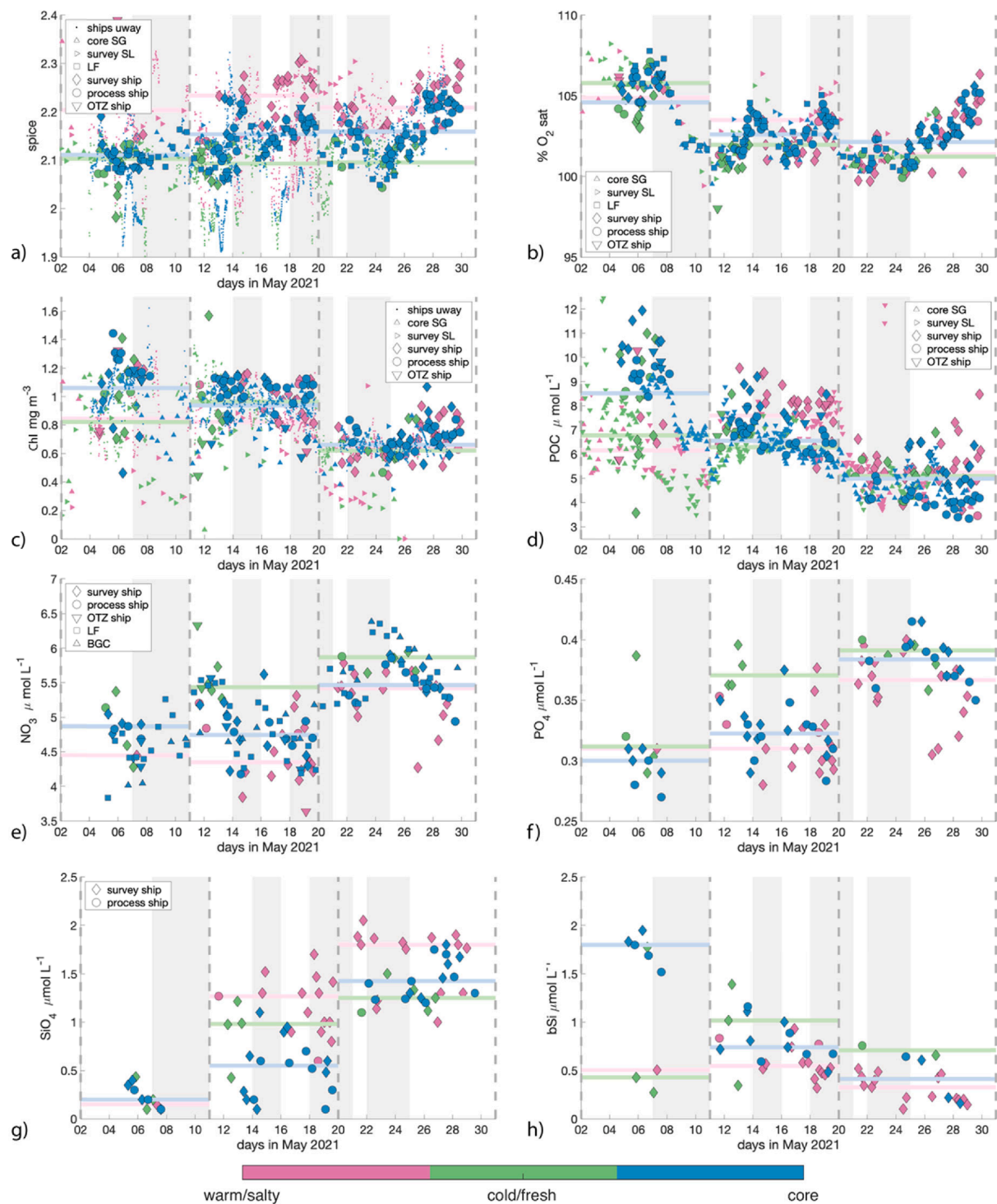
Fig. 14. ML average quantities across water masses and epochs a) Π, b) %O₂, C) Chl, d) POC, e) NO₃, f) PO₄, e) SiO₄, f) bSi. Gray shaded regions denote storm dates, and gray dashed lines delineate epochs. Epoch mean values for each water mass are given by the horizontal colored lines and the platform by the different plot symbols.

turbulent fluxes across the ML base are highly nonlinear and each method is sensitive to the choice of parameters and analysis procedures. Here, both forms in Eq. (5) will be used to calculate changes in ML quantities during each storm event to provide an estimate of how well biogeochemical entrainment rates can be constrained.

For the flux form, κ_H is taken from the ensemble of 1D models and is evaluated at 5 m below the modeled ML base (Fig. 10, Table 2). The integration occurs over the final MLD, H_f, at the end of each storm. The

gradient, $\partial \overline{C}/\partial z$ is calculated using a LOESS fit to SCW CTD nutrient profiles, collected in the five days before each storm and over the depth ΔH_E (Fig. 15a). Changes of NO₃, SiO₄ and PO₄ due to entrainment are the largest during storm three (Fig. 15b), coincident with the strongest winds and ML deepening to 80 m. Integrated entrainment due to storms inject ∼ 0.3–1 μmol/L NO₃, ∼0.3–1 μmol/L SiO₄, and 0.03–0.05 μmol/L PO₄ into the ML (see Table 5). The difference in entrainment rate, estimated from the two methods, varies by a factor of two for storms
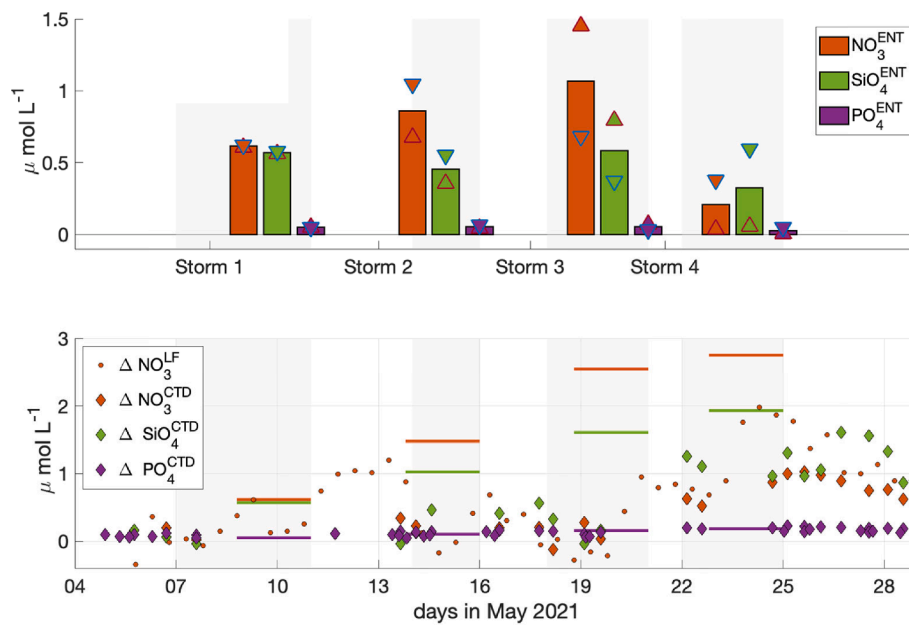
Fig. 15. Turbulent entrainment estimates at the base of the ML for SCWs: a) Total changes in nutrients due to entrainment for each storm event (shaded gray area). The triangles with red outlines are the flux form estimate, the upside-down triangles with blue outlines are the bulk estimate and the bar graph is the average of the two. Entrainment nutrients estimates were evaluated for NO_3 (orange), SiO_4 (green) and PO_4 (purple). b) Lines represent the cumulative increase in nutrients due to entrainment (i.e., sum of bars in (a)). The diamonds are the ML averaged nutrient concentrations of SCWs relative to the average nutrient concentrations during epoch 1. Dashed gray lines represent epoch boundaries. (For interpretation of the references to color in this figure legend, the reader is referred to the web version of this article.)

Table 5
Estimated total changes in ML nutrients as a result of entertainment during each storm event. Each estimate includes the flux form estimate (ΔC_{-FLUX} and triangles with red outlines in Fig. 15) and the second value is the bulk estimate (ΔC_{-BULK} and upside-down triangles with blue outlines in Fig. 15).

	Storm 1	Storm 2	Storm 3	Storm 4
ΔNO_{3-FLUX}	0.60 μmol/L	0.68 μmol/L	1.45/ μmol L^{-1}	0.04 μmol/L
ΔNO_{3-BULK}	0.62 μmol/L	1.05 μmol/L	0.68 μmol/L	0.38 μmol/L
ΔSiO_{4-FLUX}	0.56 μmol/L	0.36 μmol/L	0.79 μmol/L	0.05 μmol/L
ΔSiO_{4-BULK}	0.58 μmol/L	0.55 μmol/L	0.37 μmol/L	0.59 μmol/L
ΔPO_{4-FLUX}	0.05 μmol/L	0.04 μmol/L	0.07 μmol/L	0.01 μmol/L
ΔPO_{4-BULK}	0.05 μmol/L	0.07 μmol/L	0.03 μmol/L	0.05 μmol/L

1–3, yet varies by a factor of 10 for storm 4.

The cumulative change in nutrient concentrations due to entrainment is 2–3 times larger than the observed increase of SCW nutrients, consistent with a biologically active upper ocean that draws down the entrained nutrients and regenerates O_2 during post storm events (Fig. 15b).

Section 5 explored the role of *HORIZ* on SCW T/S variability. Though there is insufficient data to calculate horizontal nutrient gradients, and therefore advective fluxes similar to those estimated in Section 5, the weak lateral nutrient variability (a maximum difference of 1 μmol/L for SiO_4 and NO_3; Fig. 14) stands in contrast to the strong vertical nutrient gradients across the ML base (4–10 μmol/L for NO_3 and 0.3–3 μmol/L for SiO_4). This suggests that vertical mixing dominates the physically modulated changes in SCW nutrients during the field campaign. This differs from the physical properties (Section 5), where horizontal advection plays a leading order role in the T/S evolution in the SCW. The differing contributions of lateral processes to physical and biogeochemical budgets highlight the importance of both gradients and transport on the physical evolution of tracers in the SCWs.

7. Comparing oceanographic conditions during the EXPORT NA field campaign to previous years

The conditions during the EXPORTS NA field campaign were somewhat anomalous for the study site. The heat flux zero crossing in early April was consistent with previous years, and the surface net heat flux during May was typical for the region (Fig. 16). The storms experienced by the upper ocean during the field program were more intense than normal, reaching 2–3 times the mean values for May. The strong winds, even in the presence of stabilizing surface heat flux, cause deeper ML, (avg ~ 40 m) than previous years (median ~ 25 m). Though anomalous, high wind events are not totally uncommon in May. During May between 2002 and 2022, daily average τ exceeds 0.4 N m^{-2} in 15 of the 21 years analyzed, spanning a total of 39 days.

These anomalously high wind events during 2021 deepened MLs, entrained nutrients and induced Ekman currents that transported ML tracers above the eddy core waters. The advection of biogeochemical tracers by upper ocean flows is usually evaluated in the context of altimetrically derived geostrophic velocity fields; however, these results point to the importance of entrainment and Ekman driven flows in particle transport under high wind forcings. Results in sections 5 and 6 highlight the need for more understanding of how wind-driven currents impact the trajectories of near-surface tracers.

8. Conclusions

In dynamically complex regions such as the North Atlantic, retentive eddies can provide well-contained regions for the assessment of changes in upper ocean biogeochemical stocks, rates fluxes in a nearly Lagrangian frame. Logistically, this involves the ability to track the eddy center throughout a field campaign. Here, eddy tracking was accomplished through both the reference frame provided by the subsurface Lagrangian float and a dedicated eddy tracking team onshore (see Erickson et al, 2022). A sophisticated situational awareness program allowed data to be shared readily between research teams on the ships and onshore. Both the Lagrangian float and eddy tracking efforts were
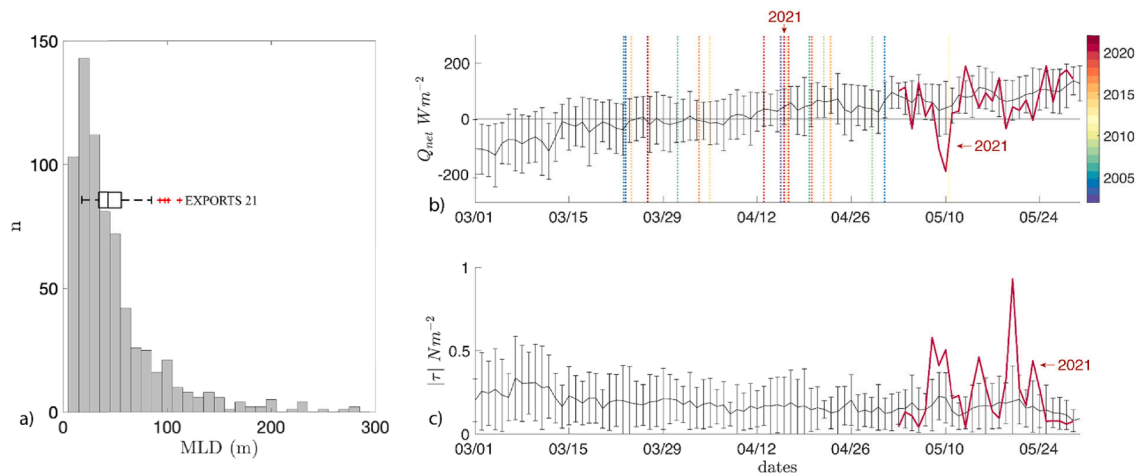
Fig. 16. A) histogram of may mlds from argo profiles near the field campaign (between−20 W to −13 W, and 47 N to 50 N) from 2006 to 2020. The box plot includes MLDs from all EXPORTS NA profiling assets. In general, storms resulted in deeper MLD than seen on average. b) Daily mean surface heat flux (and standard deviations) from ERA 5 reanalysis from 2002 to 2022. The heat flux at the field site during the 2021 EXPORTS NA field program depicted in red. Thin dashed lines are the date of zero crossing of the heat flux for each year designated by the colorbar on the right. In general the heat flux was consistent with previous years. c) Mean surface wind stress (and standard deviation) from ERA 5 reanalysis from 2002 to 2022. The wind stress at the field site during the 2021 EXPORTS NA field program is in red. Wind stress was higher than previous years and is marked by the storm events encountered during the experiment. (For interpretation of the references to color in this figure legend, the reader is referred to the web version of this article.)

necessary as the rapidly evolving mesoscale field caused periodic uncertainty in real-time eddy center estimates. The delayed time eddy center product and Lagrangian float are within 10 km of each other throughout the field campaign, confirming the success of eddy tracking efforts and is consistent with a retentive eddy core (Erickson et al, 2022).

The multi-ship, multi-asset campaign surveyed the physical and biogeochemical fields within, across, and around the single anticyclonic mode water eddy. Three gliders that surveyed the surrounding eddy field leading up to the ship-based program recorded deep wintertime ML (100–150 m) followed by basin-wide solar radiation-driven restratification and increases in evaluated $\%O_2$ and Chl through mid-April. The goal of the ship-based program that followed was to target the center of a retentive eddy and to conduct a Lagrangian assessment of changes of biogeochemical stocks, rates and fluxes within the eddy SCWs to assess the fates of the North Atlantic spring bloom. Extremely low silicate concentrations indicated that a diatom bloom had indeed occurred, while relatively high residual nitrate and orthophosphate concentrations maintained the potential for subsequent blooms of non-siliceous phytoplankton.

Geostrophic velocities and in-situ measurements confirm that the eddy contained a deep retentive core (i.e. ECWs). Yet Ekman transport and vertical mixing challenged the Lagrangian framework within the surface waters above the eddy's core (i.e. in the SCWs). The massive field campaign distributed sampling efforts to collect continuous measurements near the eddy center (core assets and process ship) and survey the surrounding physical and biogeochemical field simultaneously. The importance of these two separate efforts for understanding the role of physics in the biogeochemical fields cannot be overstated. Core assets tracked consistently the tendency of physical and bio-optical properties in the ML, while assets and ships traversing the eddy offered rich detail about the lateral structure. Combined, these provide an unprecedented opportunity to evaluate the impact of horizontal and vertical advection on water transformations near the eddy center.

Four storms brought strong westerly winds that deepened MLs by 25–40 m to as deep as 100 m and resulted in Ekman exchange in the surface layers. Estimates of flushing time scale range 5–8 days, with SCW exchange ranging 20–75 % during storms. The SCW exchange is consistent with particle tracking advected by combined geostrophic and Ekman velocities which estimate a particle retention time in the eddy of 12 days. This is less than half the retention time of 28 days estimated

using particle tracking with geostrophic velocities alone. This Ekman transport provides a mechanism for exchange between coherent eddies and surrounding waters that should be considered when evaluating eddy trapping impacts on Chl using satellite-based methods.

The largest horizontal exchange occurred during the first storm between epochs 1 and 2, which replaced much of the surface core waters with warm/salty water from outside of the eddy's core region. Each storm event resulted in the vertical entrainment of low O_2 and high nutrient water into the ML. The relative contributions of horizontal vs. vertical advection on tracer fluxes depended on the horizontal and vertical gradients of that tracer. While horizontal advection played a large role in salinity fluxes, entrainment played a larger role in the fluxes of nutrients discussed here. After each storm injected nutrients and drove down oxygen, the ML appeared to respond by driving down nutrients and driving up $\%O_2$. Overall, chlorophyll and POC were highest at the onset of the field program, and decreased throughout the campaign, particularly after storm 2 and the beginning of epoch 3 (Fig. 13, Fig. 14).

The SCW and ECW definitions here do not encompass the seasonal pycnocline, which sits between the active upper ocean and retentive interior. This region exhibits complex behavior (e.g. ML deepening and shoaling) as well as weakening stratification (e.g. Fig. 7). Further analysis into this region is beyond the scope of this work.

Satellite SST and Chl imagery highlight strong spatial variability with warm, salty chlorophyll rich water to the south that is stirred by the mesoscale circulation around the eddy periphery (Figs. 5, 6 & 9). The spatial variability of nutrients across the eddy was largest during epoch 1 for POC and Chl, but was largest in epoch 2 for NO_3 and SiO_4 (Fig. 14). Changes across water classes were not necessarily consistent. For example, Warm/Salty waters during epoch 2 are elevated in SiO_4 compared to SCWs yet are depleted in NO_3. This suggests spatial heterogeneity in biogeochemical processes across the eddy. Yet, even in the presence of spatial heterogeneity, temporal changes across epochs, marked by storms, dominated the variability of the biogeochemical tracers. This is a reminder of the complexity inherent in observing the multiple spatial and temporal scales of biophysical interaction and reinforces the strengths and novel capabilities that lead to the ability to create a physical based context for the North Atlantic EXPORTS field program.

The month-long field campaign captured the importance of physical

Table A1

EXPORTS NA Sampling Systems.

Platform	Sampling System
Process Ship - RSS James Cook (JC214)	
CTD/Rosette	CTD/Rosette with bio-optical sensors & 24 20L Niskin bottles
Underway	CTD and bio-optical sensors, hyperspectral absorption/attenuation, multispectral backscatter, fast repetition rate fluorometry, small particle imaging (Imaging Flow Cytobot [IFCB]), net community production (O_2/Ar) time series at 5-m intake depth with discrete samples
MOCNESS	Multiple opening/closing net and environmental sensing system (MOCNESS) that enables zooplankton collections using a 1 m^2 net opening in depth-discrete intervals from 0 to 1,000 m with CTD sensors
Net tows	Vertically integrated collection of live zooplankton for experimental work
Marine snow catchers	Large volume (100 L) sampling bottles that enable particles to be sorted based upon sinking speeds
Sediment traps	Neutrally buoyant and surface-tethered sediment trap arrays with polyacrylamide gel, O_2 respiration and optical sediment traps, upward looking cameras
In situ optics	Compact optical profiling system (C-OPS) spectroradiometer profiles, near-surface hyperspectral reflectance (THSRB), slow-drop inherent optical property (IOP) profiling system and multispectral backscatter
Above water optics	Hyperspectral ocean reflectance from bow-mounted system (HyperSAS)
ADCP	Acoustic Doppler Current Profilers operation at 75 and 150 kHz used to make horizontal current profiles from surface to more than 500 m (depending on weather and scatterer concentrations)
Survey Ship - RSS Discovery (DY131)	
CTD/Rosette	CTD/Rosette with bio-optical sensors & 24 20L Niskin bottles
Underway	CTD and bio-optical sensors, hyperspectral absorption/attenuation, multispectral backscatter, small particle imaging (IFCB), net community production (O_2/Ar), pH and NO_3 time series at 5 m intake depth with discrete samples
TMC CTD/Rosette	Trace metal clean (TMC) collection of discrete water samples with CTD sensors
TMC towfish	Large volume TMC collection of mixed layer water for experiments
uCTD	Fast profiling CTD
Large volume pumps	Size-fractionated, large volume particle sampling at 7–9 depths
In situ optics	C-OPS spectroradiometer profiles, THSRB hyperspectral reflectance spectra and lowering frame with hyperspectral absorption/attenuation, multispectral backscatter, small particle size distribution profiles
Above water optics	HyperSAS ocean reflectance from bow-mounted system
ADCP	Acoustic Doppler Current Profilers operation at 75 and 150 kHz used to make horizontal current profiles from surface to more than 500 m (depending on weather and scatterer concentrations)
OTZ Ship - RV Sarmiento de Gamboa (SG2105)	
CTD/Rosette	CTD/Rosette with bio-optical sensors & 24 12L Niskin bottles
MOCNESS	Multiple opening/closing net and environmental sensing system (MOCNESS) that enables zooplankton collections using a 10 m^2 net opening in depth-discrete intervals from 0 to 1,000 m with CTD sensors
Net tows	Vertically integrated collection of live zooplankton and fishes for experimental work
Stingray	Tow sled with physical sensors (T,S), bio-optical sensors (O2, Chl) and an In-Situ Ichthyoplankton Imaging System
ADCP	Acoustic Doppler Current Profilers operation at 75 and 150 kHz used to make horizontal current profiles from surface to more than 500 m (depending on weather and scatterer concentrations)
Autonomous vehicles	
Lagrangian Float	The Lagrangian float is designed to follow the motion of water parcels. A LF was deployed in the center of the eddy, below the ML and profiled from the therermocline to the surface twice a

Table A1 (*continued*)

Platform	Sampling System
	day. The LF was equipped with a CTD, O_2, chlorophyll fluorescence, and NO_3
SeaGlider	Sampling from the surface to about 1,000 m around the Lagrangian float and ships, profiles every 6 h, instrumented with CTD, O_2, optical backscatter, chlorophyll fluorescence, spectral downwelling irradiance (412, 443, 554 nm, PAR) and acoustic Doppler current profiler sensors; operational July–December 2018
BGC float	Two BGC Argo floats were deployed from the survey ship. BGC304 (wmo#1902304) was deployed in the center of the eddy while BGC303 (wmo#1902303) was deployed near the edge of the eddy. Results shown here are from BGC304. BGC304 profiled once each night, to 1000 m with every 4th profile extending down to 2000 m. Daily profiling was continued through June, after which the float profiled at 10-d intervals.
Wirewalker	Profiles every 40 min from surface to about 500 m, instrumented with CTD and O_2, optical backscatter, chlorophyll fluorescence, CDOM fluorescence, beam attenuation and PAR sensors; deployed at the start and recovered at the end of every epoch
Drifters	Surface Drifters, deployed throughout campaign (global drifter program)

processes that evolve on timescales of hours, days and weeks, yet changes in the mesoscale eddy field could play a role in biogeochemical tracer evolution on these and longer timescales. Here, the eddy evolved during the observational campaign. This is evident in the satellite images of both Chl and SST showing a circular-shaped eddy at the beginning of epoch 1 that became elongated by the end of epoch 3. Observations in Gulf Stream rings have been observed to exchange tracers between the core and surrounding waters over many months (The Ring Group, 1981). In the eddy explored here, temperature and salinity transformations of the SCWs can be explained more rapidly by surface forcing and Ekman advection. Though all in-situ metrics confirm the eddy retained its retentive core, the weakening pycnocline suggests an evolving PV structure with implications for the biophysical interaction on weekly, monthly, and longer timescales not explored here.

One of the primary goals of the EXPORTS science plan was to collect ecological and biogeochemical observations in a Lagrangian fashion over finite sampling epochs (Siegel et al. 2016). If the water column were truly Lagrangian, then the organic carbon exported from the upper ocean food web would directly feed the export flux pathways sampled at depth. The present analysis, while also summarizing the physical and biogeochemical landscape of the field site and creating oceanographic context for future studies, quantifies the degree to which the sampling conducted was truly Lagrangian. This effort also highlights the many challenges of conducting production-flux experiments even in a Lagrangian frame and calls into question the inherent uncertainties of interpreting biological carbon pump observations that were collected in a Eulerian frame of reference.

CRediT authorship contribution statement

Leah Johnson: Methodology, Formal analysis, Data curation, Investigation, Visualization. **David A. Siegel:** Conceptualization, Investigation, Methodology, Funding acquisition. **Andrew F. Thompson:** Conceptualization, Data curation, Methodology. **Erik Fields:** Data curation, Formal analysis, Visualization. **Zachary K. Erickson:** Methodology, Writing – review & editing. **Ivona Cetinic:** Conceptualization, Methodology, Investigation. **Craig M. Lee:** Conceptualization, Methodology, Investigation. **Eric A. D'Asaro:** Conceptualization, Methodology, Investigation. **Norman B. Nelson:** Data curation, Investigation. **Melissa M. Omand:** Conceptualization, Methodology. **Michaela Sten:** Data curation, Visualization. **Shawnee Traylor:** Data curation, Visualization. **David P. Nicholson:** Conceptualization, Methodology. **Jason
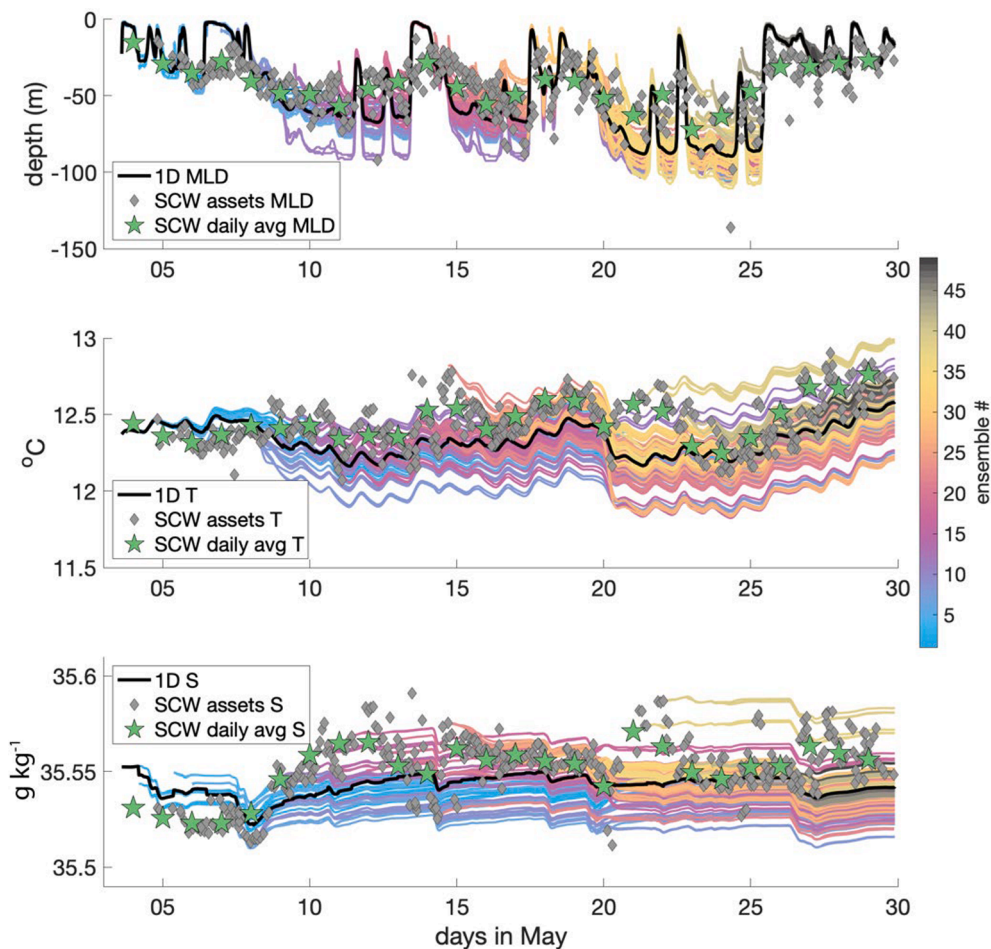
Fig. A1. Model simulation ensembles. Each color is a different simulation initialized by a glider profile.

Table A2

ML models.

model	Citation
KEPS	Rodi 1987; Umlauf, Burchard, 2003
ePBL	Reichl and Hallberg, 2018
KPP-CVMIX	VanRoekel et al, 2018

R. Graff: Conceptualization, Methodology, Investigation. **Deborah K. Steinberg:** Conceptualization, Methodology, Investigation. **Heidi M. Sosik:** Conceptualization, Methodology, Investigation, Funding acquisition. **Ken O. Buesseler:** Conceptualization, Methodology, Investigation, Funding acquisition. **Mark A. Brzezinski:** Methodology, Investigation, Data curation. **Inia Soto Ramos:** . **Filipa Carvalho:** Methodology, Writing – review & editing. **Stephanie A. Henson:** Funding acquisition, Writing – review & editing.

Declaration of Competing Interest

The authors declare that they have no known competing financial interests or personal relationships that could have appeared to influence the work reported in this paper.

Data availability

Data has been submitted to SeaBass

*Data Statement.

All NASA funded EXPORTS data is being archived at NASA's Sea-WiFS Bio-optical Archive and Storage System (SeaBASS) under the EXPORTS Experiment (10.5067/SeaBASS/EXPORTS/DATA001). Data collected during the EXPORTSNA field expedition onboard the Sarmiento the Gamboa was archived under the OTZ_WHOI experiment (10.5067/SeaBASS/OTZ_WHOI/DATA001) and cruise name SG2105. All CTD and nutrient data can be found under Principal Investigator (PI) Norman Nelson, Lagrangian Float data under PI Eric D'Asaro, and Glider data under PI Craig Lee. A curated dataset with all the data used for this manuscript was archived under the main author's (SeaBASS investigator) Leah Johnson and experiments (DOI's) EXPORTS and OTZ_WHOI. To access the data in SeaBASS, search for investigator Leah Johnson and download the files and associated documents for each DOI. BGC Argo floats data is publicly available at https://biogeochemical-argo.org/data-access.ph

Appendix A

See Table A1

Appendix B

Competition between turbulent mixing driven by winds and surface cooling, and buoyancy input from warming, freshwater fluxes and entrainment fluxes at the ML base drives ML deepening (e.g. Kraus and Turner 1967, Reichl and Hallberg, 2018, VanRoekel et al, 2018, Umlauf, Burchard, 2003). This study explores the impact of vertical mixing on the surface ocean using three different SC models within the common framework GOTM (Umlauf and Burchard, 2005). The list of parameterizations used in this study and the references are summarized in Table A1.

The simulations were run with a uniform vertical grid spacing of 0.5 m, a time step of 60 s and initialized with profiles of mean T and S from the core SG. Radiative heat fluxes, wind stress and freshwater fluxes used to force the simulations were derived using COARE 3.5 with meteorological fields from the DY131. If DY131 meteorological data was unavailable, ERA-5 reanalysis was used. An ensemble of models is used to a) evaluate the sensitivity of SC model turbulence parameterization choice (e.g. Li, 2019, Johnson et al., 2023) (Fig. A1) and b) to gauge the uncertainty in approximating 1D physics in the eddy center. To address (a), GOTM was run using three different turbulence parameterizations (Table A2), used commonly in regional and global circulation models. To address (b), 1D models were initialized with each core SG profile, resulting in 96 simulations for each model approximately 6 h apart (i.e. length between seaglider dives). Combined, a total of 288 SC model simulations were run from 5/4–5/30. The spread among models provides uncertainty in the 1D estimate when using it to understand spatial variability as discussed in section 5 and is used to estimate error bars on Figs. 10 and 11.

References

Alkire, M.B., Lee, C., D'Asaro, E., Perry, M.J., Briggs, N., Cetinić, I., Gray, A., 2014. Net community production and export from S eaglider measurements in the N orth A tlantic after the spring bloom. J. Geophys. Res. Oceans 119 (9), 6121–6139.

Boyd, P.W., Claustre, H., Levy, M., Siegel, D.A., Weber, T., 2019. Multi-faceted particle pumps drive carbon sequestration in the ocean. Nature 568, 327–335.

Cetinić, I., Perry, M.J., Briggs, N.T., Kallin, E., D'Asaro, E.A., Lee, C.M., 2012. Particulate organic carbon and inherent optical properties during 2008 North Atlantic Bloom Experiment. J. Geophys. Res. Oceans 117 (C6).

Cetinić, I., Perry, M.J., D'asaro, E., Briggs, N., Poulton, N., Sieracki, M.E., Lee, C.M., 2015. A simple optical index shows spatial and temporal heterogeneity in phytoplankton community composition during the 2008 North Atlantic Bloom Experiment. Biogeosciences 12 (7), 2179–2194.

Dam, H.G., Miller, C.A., Jonasdottir, S.H., 1993. The trophic role of mesozooplankton at 47 N, 20 W during the north atlantic bloom experiment. Deep Sea Res. Part II 40 (1–2), 197–212.

de Boyer Montégut, C., Madec, G., Fischer, A.S., Lazar, A., Iudicone, D., 2004. Mixed layer depth over the global ocean: An examination of profile data and a profile-based climatology. J. Geophys. Res. Oceans 109 (C12).

DeVries, T., 2022. The ocean carbon cycle. Annu. Rev. Env. Resour. 47, 317–341.

Erickson, Z.K., E. Fields, M.M. Omand, L. Johnson, A.F. Thompson, E. D'Asaro, F. Carvalho, L.A. Dove, C.M. Lee, D.P. Nicholson, G. Shilling, I. Cetinić and D. Siegel. (2022), EXPORTS North Atlantic Eddy Tracking. NASA Technical Memorandum, NASA/TM-20220009705, https://ntrs.nasa.gov/api/citations/20220009705/downloads/NASA%20TM%2020220009705.pdf.

Erickson, Z.K., Fields, E., Johnson, L., Thompson, A.F., Dove, L.A., D'Asaro, E., Siegel, D. A., 2023. Eddy tracking from in situ and satellite observations. J. Geophys. Res. Oceans.

Hartman, S.E., Bett, B.J., Durden, J.M., Henson, S.A., Iversen, M., Jeffreys, R.M., Horton, T., Lampitt, R., Gates, A.R., 2021. Enduring science: three decades of observing the northeast atlantic from the porcupine abyssal plain sustained observatory (PAP-SO). Prog. Oceanogr. 191, 102508.

Henson, S.A., Sanders, R., Holeton, C., Allen, J.T., 2006. Timing of nutrient depletion, diatom dominance and a lower-boundary estimate of export production for Irminger Basin, North Atlantic. Mar. Ecol. Prog. Ser. 313, 73–84.

Hersbach, H., Bell, B., Berrisford, P., Hirahara, S., Horányi, A., Muñoz-Sabater, J., Nicolas, J., Peubey, C., Radu, R., Schepers, D., Simmons, A., Soci, C., Abdalla, S., Abellan, X., Balsamo, G., Bechtold, P., Biavati, G., Bidlot, J., Bonavita, M., De Chiara, G., Dahlgren, P., Dee, D., Diamantakis, M., Dragani, R., Flemming, J., Forbes, R., Fuentes, M., Geer, A., Haimberger, L., Healy, S., Hogan, R.J., Hólm, E., Janisková, M., Keeley, S., Laloyaux, P., Lopez, P., Lupu, P., Radnoti, G., de Rosnay, P., Rozum, I., Vamborg, F., Villaume, S., Thépaut, J.N., 2020. The ERA5 global reanalysis. Q. J. R. Meteorolog. Soc. 146 (730), 1999–2049.

Johnson, L., Fox-Kemper, B., Li, Q., Pham, H.T., Sarkar, S., 2023. A finite time ensemble method for mixed layer model comparison. Journal of Physical. Oceanoography.

Johnson, L., Lee, C.M., D'Asaro, E.A., 2016. Global estimates of lateral springtime restratification. J. Phys. Oceanogr. 46 (5), 1555–1573.

Kraus, E.B., Turner, J.S., 1967. A one-dimensional model of the seasonal thermocline II. The general theory and its consequences. Tellus 19 (1), 98–106.

Leblanc, K., Hare, C.E., Feng, Y., Berg, G.M., DiTullio, G.R., Neeley, A., Leblanc, K., Hare, C.E., Feng, Y., Berg, G.M., DiTullio, G.R., Neeley, A., Benner, I., Sprengel, C., Beck, A., Sanudo-Wilhelmy, S.A., Passow, U., Klinck, K., Rowe, J.M., Wilhelm, S.W., Brown, C.W., Hutchins, D.A., 2009. Distribution of calcifying and silicifying phytoplankton in relation to environmental and biogeochemical parameters during the late stages of the 2005 North East Atlantic Spring Bloom. Biogeosciences 6 (10), 2155–2179.

Lehahn, Y., d'Ovidio, F., Lévy, M., Heifetz, E., 2007. Stirring of the northeast Atlantic spring bloom: A Lagrangian analysis based on multisatellite data. J. Geophys. Res. Oceans 112 (C8).

Lochte, K., Ducklow, H.W., Fasham, M.J.R., Stienen, C., 1993. Plankton succession and carbon cycling at 47 N 20 W during the JGOFS north atlantic bloom experiment. Deep Sea Res. Part II 40 (1–2), 91–114.

MacGilchrist, G.A., Marshall, D.P., Johnson, H.L., Lique, C., Thomas, M., 2017. Characterizing the chaotic nature of ocean ventilation. J. Geophys. Res. Oceans 122 (9), 7577–7594.

Mahadevan, A., D'asaro, E., Lee, C., Perry, M.J., 2012. Eddy-driven stratification initiates North Atlantic spring phytoplankton blooms. Science 337 (6090), 54–58.

Martin, P., Lampitt, R.S., Jane Perry, M., Sanders, R., Lee, C., D'Asaro, E., 2011. Export and mesopelagic particle flux during a North Atlantic spring diatom bloom. Deep Sea Res.,Part I 58 (4), 338–349. https://doi.org/10.1016/j.dsr.2011.01.006.

McDougall, T.J., Barker, P.M., 2011. Getting started with TEOS-10 and the Gibbs Seawater (GSW) oceanographic toolbox. Scor/iapso WG 127 (532), 1–28.

McNair, H., M. Meyer, S. Lerch, A.E. Maas, B. Stephens, J. Fox, K.N. Buck, S.M. Burns, I. Cetinić, M. Cohn, C. Durkin, S. Gifford, W. Gong, J. R. Graff, B. Jenkins, E.L. Jones, A.E. Santoro, C.H. Shea, K. Stamieszkin, D.K. Steinberg, A. Marchetti, C.A. Carlson, S. Menden-Deuer, M.A. Brzezinski, D.A. Siegel, and T. Rynearson. (2023). Quantitative analysis of food web dynamics in a low export ecosystem. Preprint available at bioRxiv. 2023.03.17.532807; 10.1101/2023.03.17.532807.

Monin, A.S., Obukhov, A.M., 1954. Basic laws of turbulent mixing in the surface layer of the atmosphere. Contrib. Geophys. Inst. Acad. Sci. USSR 151 (163), e187.

Mousing, E.A., Richardson, K., Bendtsen, J., Cetinić, I., Perry, M.J., 2016. Evidence of small-scale spatial structuring of phytoplankton alpha-and beta-diversity in the open ocean. J. Ecol. 104 (6), 16821695.

Nowicki, M., DeVries, T., Siegel, D.A., 2022. Quantifying the carbon export and sequestration pathways of the ocean's biological carbon pump. Global Biogeochem. Cycles. https://doi.org/10.1029/2021GB007083.

Omand, M.M., D'Asaro, E.A., Lee, C.M., Perry, M.J., Briggs, N., Cetinić, I., Mahadevan, A., 2015. Eddy-driven subduction exports particulate organic carbon from the spring bloom. Science 348 (6231), 222–225.

Reichl, B.G., Hallberg, R., 2018. A simplified energetics based planetary boundary layer (ePBL) approach for ocean climate simulations. Ocean Model. 132, 112–129.

Ring Group, T., 1981. Gulf Stream cold-core rings: Their physics, chemistry, and biology. Science 212 (4499), 1091–1100.

Rodi, W., 1987. Examples of calculation methods for flow and mixing in stratified fluids. J. Geophys. Res. Oceans 92 (C5), 5305–5328.

Rumyantseva, A., Henson, S., Martin, A., Thompson, A.F., Damerell, G.M., Kaiser, J., Heywood, K.J., 2019. Phytoplankton spring bloom initiation: The impact of atmospheric forcing and light in the temperate North Atlantic Ocean. Prog. Oceanogr. 178, 102202.

Siegel, D.A., Buesseler, K.O., Behrenfeld, M.J., Benitez-Nelson, C., Boss, E., Brzezinski, M. A., Burd, A.B., Carlson, C.A., D'Asaro, E.A., Doney, S.C., Perry, M.J., Stanley, R.H.R., Steinberg, D.K., 2016. Prediction of the export and fate of global ocean net primary production: The EXPORTS science plan, frontiers in marine. Science 3 (22). https://doi.org/10.3389/fmars.2016.00022.

Siegel, D.A., Cetinić, I., Graff, J.R., Lee, C.M., Nelson, N., Perry, M.J., Soto Ramos, I., Steinberg, D.K., Buesseler, K., Hamme, R., Fassbender, A.J., Nicholson, D., Omand, M.M., Robert, M., Thompson, A., Amaral, V., Behrenfeld, M., Benitez-Nelson, C., Bisson, K., Boss, E., Boyd, P.W., Brzezinski, M., Buck, K., Burd, A., Burns, S., Caprara, S., Carlson, C., Cassar, N., Close, H., D'Asaro, E., Durkin, C., Erickson, Z., Estapa, M.L., Fields, E., Fox, J., Freeman, S., Gifford, S., Gong, W., Gray, D., Guidi, L., Haëntjens, N., Halsey, K., Huot, Y., Hansell, D., Jenkins, B., Karp-Boss, L., Kramer, S., Lam, P., Lee, J.-M., Maas, A., Marchal, O., Marchetti, A., McDonnell, A., McNair, H., Menden-Deuer, S., Morison, F., Niebergall, A.K., Passow, U., Popp, B., Potvin, G., Resplandy, L., Roca-Martí, M., Roesler, C., Rynearson, T., Traylor, S., Santoro, A., Duncan Seraphin, K., Sosik, H.M., Stamieszkin, K., Stephens, B., Tang, W., Van Mooy, B., Xiong, Y., Zhang, X., 2021. An operational overview of the EXport processes in the ocean from remote sensing (EXPORTS) northeast pacific field deployment. Elem. Sci. Anth. https://doi.org/10.1525/elementa.2020.00107.

Siegel, D.A., DeVries, T., Cetinić, I., Bisson, K.M., 2023b. Quantifying the ocean's biological pump and its carbon cycle impacts on global scales. Annual Review of Marine Sciences. https://doi.org/10.1146/annurev-marine-040722-115226.

Siegel, D. A., Cetinić, I., Thompson, A. F., Nelson, N. B., Sten, M., Omand, M. M., Traylor, S., Nicholson, .D P., D'Asaro, E. A., Zhang, X., Erickson, Z. K., Johnson, L., Soto Ramos, I., 2023, EXport Processes in the Ocean from RemoTe Sensing (EXPORTS) North Atlantic sensor calibration and intercalibration documents. 10.1575/1912/66998.

Sieracki, M.E., Verity, P.G., Stoecker, D.K., 1993. Plankton community response to sequential silicate and nitrate depletion during the 1989 North Atlantic spring bloom. Deep Sea Res. Part II 40 (1–2), 213–225.

Stamieszkin, K., Steinberg, D.K., Maas, A.E., 2021. Fecal pellet production by mesozooplankton in the subarctic Northeast Pacific Ocean. Limnol. Oceanogr. 66, 2585–2597. https://doi.org/10.1002/lno.11774.

Steinberg, D.K., Stamieszkin, K., Maas, A.E., Durkin, C.A., Passow, U., Estapa, M.L., et al., 2022. The outsized role of salps in carbon export in the subarctic Northeast Pacific Ocean. *Global Biogeochem. Cycles* 36. https://doi.org/10.1029/2022GB007523.

Thompson, A.F., Lazar, A., Buckingham, C., Garabato, A.C.N., Damerell, G.M., Heywood, K.J., 2016. Open-ocean submesoscale motions: A full seasonal cycle of mixed layer instabilities from gliders. J. Phys. Oceanogr. 46 (4), 1285–1307.

Umlauf, L., Burchard, H., 2003. A generic length-scale equation for geophysical turbulence models. J. Mar. Res. 61 (2), 235–265.

Umlauf, L., Burchard, H., 2005. Second-order turbulence closure models for geophysical boundary layers. A review of recent work. Cont. Shelf Res. 25 (7–8), 795–827.

Van Roekel, L., Adcroft, A.J., Danabasoglu, G., Griffies, S.M., Kauffman, B., Large, W., Schmidt, M., 2018. The KPP boundary layer scheme for the ocean: Revisiting its formulation and benchmarking one-dimensional simulations relative to LES. J. Adv. Model. Earth Syst. 10 (11), 2647–2685.

Zhang, Z., Qiu, B., Klein, P., Travis, S., 2019. The influence of geostrophic strain on oceanic ageostrophic motion and surface chlorophyll. Nat. Commun. 10 (1), 2838.